Astronomy & Astrophysics

Diagnostics of irradiated gas in galaxy nuclei

I. A far-ultraviolet and X-ray dominated region code*

R. Meijerink[1] and M. Spaans[2]

[1] Sterrewacht Leiden, PO Box 9513, 2300 RA Leiden, The Netherlands
  e-mail: meijerin@strw.leidenuniv.nl
[2] Kapteyn Astronomical Institute, PO Box 800, 9700 AV Groningen, The Netherlands

Abstract. We present a far-ultraviolet (PDR) and an X-ray dominated region (XDR) code. We include and discuss thermal and chemical processes that pertain to irradiated gas. An elaborate chemical network is used and a careful treatment of PAHs and H_2 formation, destruction and excitation is included. For both codes we calculate four depth-dependent models for different densities and radiation fields, relevant to conditions in starburst galaxies and active galactic nuclei. A detailed comparison between PDR and XDR physics is made for total gas column densities between $\sim 10^{20}$ and $\sim 10^{25}$ cm^{-2}. We show cumulative line intensities for a number of fine-structure lines (e.g., [CII], [OI], [CI], [SiII], [FeII]), as well as cumulative column densities and column density ratios for a number of species (e.g., CO/H_2, CO/C, HCO$^+$/HCN, HNC/HCN). The comparison between the results for the PDRs and XDRs shows that column density ratios are almost constant up to $N_H = 10^{22}$ cm^{-2} for XDRs, unlike those in PDRs. For example, CO/C in PDRs changes over four orders of magnitude from the edge to $N_H = 10^{22}$ cm^{-2}. The CO/C and CO/H_2 ratios are lower in XDRs at low column densities and rise at $N_H > 10^{23}$ cm^{-2}. At most column densities $N_H > 10^{21.5}$ cm^{-2}, HNC/HCN ratios are lower in XDRs too, but they show a more moderate increase at higher N_H.

Key words. astrochemistry – galaxies: starburst – galaxies: active

1. Introduction

Gas clouds in the inner kpc of many galaxies are exposed to intense radiation, which can originate from an active galactic nucleus (AGN), starburst regions or both. O and B stars dominate the radiation from starbursts, which is mostly in the far-ultraviolet ($6.0 < E < 13.6$ eV), turning cloud *surfaces* into Photon Dominated Regions (PDRs, Tielens & Hollenbach 1985). Hard X-rays ($E > 1$ keV) from black hole environments (AGN) penetrate deep into cloud *volumes* creating X-ray Dominated Regions (XDRs, Maloney et al. 1996). For each X-ray energy there is a characteristic depth where photon absorption occurs. So for different spectral shapes, one has different thermal and chemical structures through the cloud. Although one source can dominate energetically over the other (e.g., an AGN in NGC 1068 or a starburst in NGC 253), the very different physics (surface vs. volume) requires that both should be considered simultaneously in each galaxy.

In PDRs and XDRs, the chemical structure and thermal balance are completely determined by the radiation field. Therefore, PDRs and XDRs are direct manifestations of the energy balance of interstellar gas and their study allows one to determine how the ISM survives the presence of stars and AGN (Tielens & Hollenbach 1985; Boland & de Jong 1982; van Dishoeck & Black 1988; Le Bourlot et al. 1993; Wolfire et al. 1993; Spaans et al. 1994; Sternberg & Dalgarno 1995; Stoerrzer et al. 1998; Spaans 1996; Bertoldi & Draine 1996; Maloney et al. 1996; Lee et al. 1996; Kaufman et al. 1999; Le Petit et al. 2002, and references therein).

PDRs and XDRs have become increasingly important as diagnostic tools of astrophysical environments with the advent of infrared and (sub-)millimetre telescopes. PDRs emit fine-structure lines of [CI] 609, [CII] 158 and [OI] 63 μm; rotational lines of CO; ro-vibrational and pure rotational lines of H_2; many H_2O lines as well as many broad mid-IR features associated with Polycylic Aromatic Hydrocarbons (PAHs). In PDRs, the bulk of H_2 is converted into atomic hydrogen at the edge and CO to neutral carbon into ionised carbon. XDRs emit brightly in the [OI] 63, [CII] 158, [SiII] 35, and the [FeII] 1.26, 1.64 μm lines as well as the 2 μm ro-vibrational H_2 transitions. The abundance of neutral carbon in XDRs is elevated compared to that in PDRs and the chemical transitions from H to H_2 and C$^+$ to C to CO are smoother (Maloney et al. 1996).

In this paper, we compare a far-ultraviolet and X-ray dominated region code. For the PDR and XDR, we discuss the cooling, heating and chemical processes. Then we show four

---

* All Appendices are only available in electronic form at
http://www.edpsciences.org

models with different radiation fields and densities, for a semi-infinite slab geometry and irradiation from one side without geometrical dilution. We conclude with a comparison between the column densities, integrated line fluxes and abundance ratios. We will apply this tool to the centres of nearby active galaxies in subsequent papers. These codes can be used over a broad range of physical situations and scales, e.g., young stellar objects, planetary nebulae or gas outflow in galaxy clusters.

2. The photon dominated region model

The global properties of PDRs are determined by a number of physical processes:

 i. Heating through photo-electric emission by dust grains and PAHs (cf. Bakes & Tielens 1994; Weingartner & Draine 2001).
 ii Heating by FUV pumping of H_2, followed by collisional de-excitation (cf. Hollenbach & McKee 1979).
 iii. Heating by cosmic rays (cf. Field 1969).
 iv. Fine-structure line cooling of [CI] 609, [CII] 158, [OI] 146 and 63 μm (cf. Tielens & Hollenbach 1985; Spaans et al. 1994).
 v. Molecular line cooling by warm molecular gas containing CO, H_2, H_2O, OH and CH (cf. Neufeld et al. 1995; Spaans & Silk 2000).
 vi. Ion-molecule reactions driven by the ionisation degree of $\sim 10^{-4}$ maintained by the ionisation of carbon in the FUV (cf. Black & Dalgarno 1977; van Dishoeck & Black 1986).
 vii. The ionisation balance of atomic gas under the influence of photo-ionisation reactions driven by FUV photons and counteracting recombination and charge transfer reactions with metals and particularly PAHs (cf. Lepp & Dalgarno 1988; Bakes & Tielens 1994).

As one moves into a PDR the extinction along the line of sight increases and the impinging radiation field is attenuated. Consequently, there are two zones over which the chemical composition of the PDR changes in a fundamental way. The first fundamental change occurs at the edge of the PDR as atomic hydrogen is converted into H_2 because the Lyman and Werner electronic bands that lead to dissociation of the H_2 molecule in the FUV become optically thick (so-called self-shielding). Deeper into the PDR, at about 3 mag of extinction, ionised carbon is quickly converted into neutral form as the FUV flux decreases due to dust absorption. C is subsequently transformed into CO, since the FUV field is reduced by grain opacity, H_2 shielding and some CO self-shielding.

The first few magnitudes of extinction of the PDR are usually referred to as the radical region since many carbon hydrides and their ions, e.g., CH, CH^+, CN, HCN, HCO^+ (and also CO^+), reach their peak abundance there, caused by the presence of both C^+ and H_2 and the high ($\sim 10^2-10^3$ K) temperatures. Ion-molecule reactions take place that lead to the formation of a large number of different molecular species. Many of the atoms and molecules in the radical region of a PDR are collisionally excited at the ambient densities and temperatures, and emit brightly in the mid-IR, FIR, millimetre and sub-millimetre.

Table 1. Adopted model parameters.

Model	G_0	F_{FUV} [erg cm^{-2} s^{-1}]	n_{H} [cm^{-3}]
1	10^3	1.6	10^3
2	10^5	160	10^3
3	10^3	1.6	$10^{5.5}$
4	10^5	160	$10^{5.5}$
δv_{d} (km s^{-1})	2.7		
δ_{d}	1.0		

The global characteristics of any PDR are defined by a few key parameters:

 i. The strength of the impinging radiation field, G_0 or I_{UV}, in units of the Habing (1969) or Draine (1978) radiation field, respectively, determines the total available radiative flux at the edge of the PDR.
 ii. The temperature and the ambient hydrogen density, $n_{\mathrm{H}} = n(\mathrm{H}) + 2n(\mathrm{H_2})$, sets to a large extent the pace of the chemical reactions and the excitation rates of the coolants.
 iii. The metallicity Z, in units of the solar value $Z_\odot$, constrains the total abundances possible for carbon- and oxygen-bearing species and hence influences the chemical and thermal structure.
 iv. The spectral shape of the impinging radiation field, parameterised by the colour temperature T_{eff} for black bodies or the frequency slope for power laws, fixes the distribution of photon flux over energy.

The details about the thermal and chemical processes we use in the code are discussed in the appendices. In the rest of the paper we use G_0, the Habing flux, as the normalisation in which we express the incident FUV radiation field, where $G_0 = 1$ corresponds to a flux of 1.6×10^{-3} erg cm^{-2} s^{-1}.

3. PDR test models

In this section, we discuss the results for four PDR models in which we have varied the radiation field G_0 and the density n_{H}. The models are for a semi-infinite slab geometry, but the code also allows for two-sided slab geometries. The adopted model parameters are listed in Table 1. Models 2 and 4 will be shown in a paper by Röllig et al (in prep.), where they are used to compare 12 different PDR codes that are commonly used. The parameters are listed in Table 1. These values are typical for the high density, strong radiation field conditions we want to investigate in, e.g., a starburst.

The fixed gas-phase and total abundances we use are given in Table 2. The total abundances are the average values of Asplund et al. (2004) and Jenkins (2004). To calculate the gas-phase abundances, we use the depletion factors calculated by Jenkins (2004).

Table 2. Abundances.

Species	$\mathcal{A}_i$(gas)	δ_i	$\mathcal{A}_i$(total)
He[a,c]	8.5×10^{-2}	1.0	8.5×10^{-2}
C	1.4×10^{-4}	0.6	2.5×10^{-4}
N	5.2×10^{-5}	0.7	7.2×10^{-5}
O	3.4×10^{-4}	0.7	4.7×10^{-4}
Si	1.7×10^{-6}	0.05	3.4×10^{-5}
S	6.9×10^{-6}	0.5	1.4×10^{-5}
Cl	5.4×10^{-8}	0.2	2.4×10^{-7}
Fe	2.0×10^{-7}	0.007	2.8×10^{-5}
P[b,c]	3.9×10^{-8}	0.1	2.9×10^{-7}
Na	5.9×10^{-7}	0.4	1.5×10^{-6}
Mg	2.7×10^{-7}	0.08	3.4×10^{-6}
Ne[c]			6.9×10^{-5}
Al			2.3×10^{-6}
Ar			1.5×10^{-6}
Ca			2.0×10^{-6}
Cr			4.4×10^{-7}
Ni			1.7×10^{-6}

Notes:
[a] Present in both PDR and XDR chemical network.
[b] Present in PDR chemical network.
[c] Used to calculate σ_{pa} for XDR.

3.1. Heating and cooling

For both radiation fields and densities, the dominant source heating to a column density $N_H \approx 10^{22}$ cm^{-2} is photo-electric emission from grains. In the moderately low density, low radiation-field Model 1, viscous heating is about equally important in this range. For Model 2 where the radiation field is increased, it contributes somewhat more than 10 percent. For the low radiation-field, high density Model 3, carbon ionisation is the second most important heating source. In Model 4, where the radiation field is increased compared to Model 3, H_2 pumping is the second most important. At high column densities ($N_H > 22.5$ cm^{-2}), [OI] 63 μm absorption and gas-grain heating are important. For the low density PDRs Model 1 and 2, only [OI] 63 μm dominates. When the density is increased in Models 3 and 4, gas-grain heating is equally important if not dominant. Other heating processes contribute less than 10 percent, but are sometimes important in determining the thermal balance.

In all models [OI] 63 μm cooling dominates to $N_H = 10^{21.5}$ cm^{-2}. In the low density PDRs, [CII] 158 μm cooling contributes more than ten percent of the cooling in this range, whereas at high densities, gas-grain cooling is the second most important coolant. In the high density, high radiation-field Model 4, this contribution can be almost forty percent. Deeper in the cloud, [CI] 610 μm and CO line cooling become important. H_2 line cooling can contribute up to

10 percent of the total cooling rate at some point, but is always a minor coolant.

3.2. Chemical and thermal structure

The $H \rightarrow H_2$ and $C^+ \rightarrow C \rightarrow CO$ transitions are quite sharp. Their actual location varies greatly, since this is strongly dependent on density and radiation field. Exposed to stronger radiation fields, the transitions occur deeper in the cloud, since the photo-dissociation rates are larger. At higher densities, the transitions occur closer to the surface of the cloud, since the recombination rates scale as n^2. For the same reason, the H^+ and O^+ fractional abundances are systematically higher in the low density models. SiO and CS are more abundant and formed closer to the surface in the high density models, which is also the case for HCO^+, HCN, HNC and C_2H.

The edge temperatures (see Fig. 6) are affected most by the strength of the radiation field when the density is largest. At a density of $n_H = 10^{5.5}$ cm^{-3}, the difference is a factor of thirty for an increase from $G_0 = 10^3$ to $G_0 = 10^5$. In the low density case this is only a factor of two. Because of optical depth effects, CO cooling is less effective at high column densities. For this reason, temperatures rise again at $N_H \approx 10^{22}$ cm^{-2} in the low density models.

4. The X-ray dominated region model

Unlike PDRs, XDRs are mostly heated by direct photo-ionisation of the gas, which produces fast electrons that lose energy through collisions with other electrons, as well as H and H_2. These fast electrons collisionally excite H and H_2, which subsequently emit Lyman α and Lyman-Werner band photons, respectively. These photons in turn are capable of ionising atoms such as C and Si or ionise and dissociate molecules such as H_2 and CO.

Compared to PDRs, the following processes play a role in XDRs (cf. Maloney et al. 1996), in part because of the production of UV photons as described above:

i. Photo-ionisation heating (i.e., Coulomb heating with thermal electrons) dominates by a large factor over the heating through photo-electric emission by dust grains and PAHs (cf. Maloney et al. 1996; Bakes & Tielens 1994).
ii. Emission from meta-stable lines of [CI] 9823, 9850 Å and [OI] 6300 Å; fine-structure line cooling of [CII] 158 and [OI] 63 and 146 μm as well as Lyman α emission (cf. Maloney et al. 1996; Tielens & Hollenbach 1985; Spaans et al. 1994).
iii. Molecular line cooling by warm molecular gas containing CO, H_2, H_2O and OH as well as gas-grain cooling where warm gas is cooled at the surfaces of lower temperature dust grains (cf. Neufeld et al. 1995; Spaans & Silk 2000).
iv. Ion-molecule reactions driven by the ionisation degree of $\sim 10^{-4}$ maintained by the ionisation of carbon in the FUV (cf. Black & Dalgarno 1977; van Dishoeck & Black 1986).
v. The ionisation balance of atomic gas under the influence of photo-ionisation reactions driven by X-ray photons
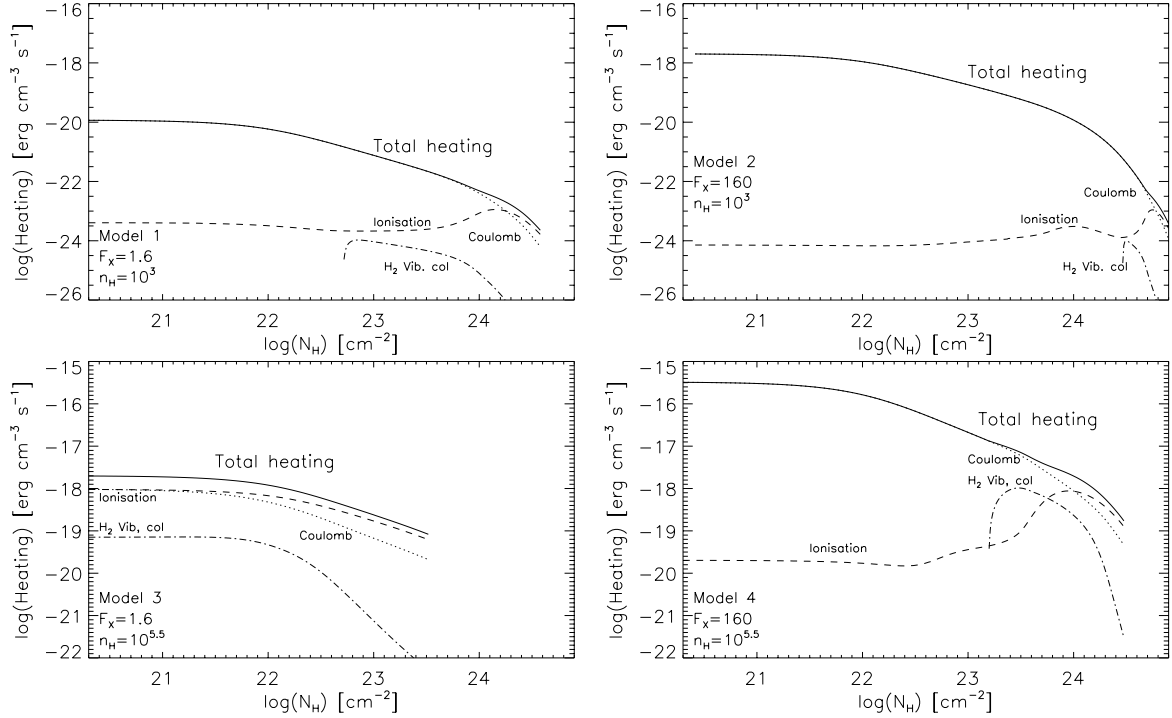
Fig. 1. Important heating processes for Model 1 (*top left*), 2 (*top right*), 3 (*bottom left*) and 4 (*bottom right*).

and charge transfer. Recombination of ions on grain surfaces is a major ionic loss route at electron fractions less than 10^{-3} (cf. Lepp & Dalgarno 1988; Bakes & Tielens 1994; Maloney et al. 1996).

The global structure of any XDR is defined by a few key parameters: the density n_H and the energy deposition rate H_X (see Appendix E) per hydrogen atom. Because the heating in XDRs is driven by photo-ionisation, the heating efficiency is close to unity as opposed to that in PDRs where the photo-electric heating efficiency is of the order of $0.3-1.0\%$ (Maloney et al. 1996; Bakes & Tielens 1994). Unlike PDRs, XDRs are exposed to X-rays as well as FUV photons.

As one moves into the XDR, X-ray photons are attenuated due to atomic electronic absorptions. The lowest energy photons are attenuated most strongly, which leads to a dependence of the X-ray heating and ionisation rates at a given point on the slope of the X-ray spectrum. We assume, for energies between 0.1 and 10 keV, that the primary ionisation rate of hydrogen is negligible compared to the secondary ionisation rate and that Auger electrons contribute an energy that is equal to the photo-ionisation threshold energy (Voit 1991).

The treatment is described in the Appendices and follows, in part, the unpublished and little-known work by Yan (1997). Also, we extend the work of Maloney et al. (1996) in terms of depth dependence, H_2 excitation and extent of the chemical network.

5. XDR test models

In this section, we consider four models with the same energy inputs and densities as the PDRs in Table 1. The spectral energy distribution is of the form $\exp(-E/1\,\text{keV})$. The energy is

emitted between 1 and 10 keV and F_{FUV} should be replaced by F_X in Table 1. This spectral shape and spectral range can be changed depending on the application. We take the parameters for the 1 keV electron to determine the electron energy deposition, since these parameters do not change for higher energies. When the spectral energy distribution is shifted towards higher energies, the X-rays will dominate a larger volume, since the absorption cross sections are smaller for higher energies. H_X/n is the most important parameter for the chemical and thermal balance, where H_X is the energy deposition rate per hydrogen nucleus. The abundances used are given in Table 2. The elements H, He, C, N, O, Si, S, Cl and Fe are included in the chemical network. The other elements listed are only used to calculate the photoelectric absorption cross section, σ_{pa}.

5.1. Heating and cooling

In Fig. 1, the different heating sources are shown as a function of the total hydrogen column density, N_H. All heating is done by X-rays, but the way it is transfered to the gas depends on the ionisation fraction. When the gas is highly ionised, $x_e \sim 0.1$, most ($\sim 70\%$) of the kinetic energy of the non-thermal electrons goes into Coulomb heating, which is the case in Models 1, 2 and 4 where H_X/n is high to $N_H > 10^{23}$ cm^{-2}. For smaller ionisation fractions, $x_e \sim 10^{-4}$, ionisation heating as discussed in Sect. B.2 is important or even dominant. In Model 3, ionisation heating and Coulomb heating are equally important at $N_H < 10^{21.8}$ cm^{-2}. In all models ionisation heating dominates especially at high column densities. When the excitation of H_2 is dominated by non-thermal processes, collisional quenching of H_2 can heat the gas. Naively, one would expect this
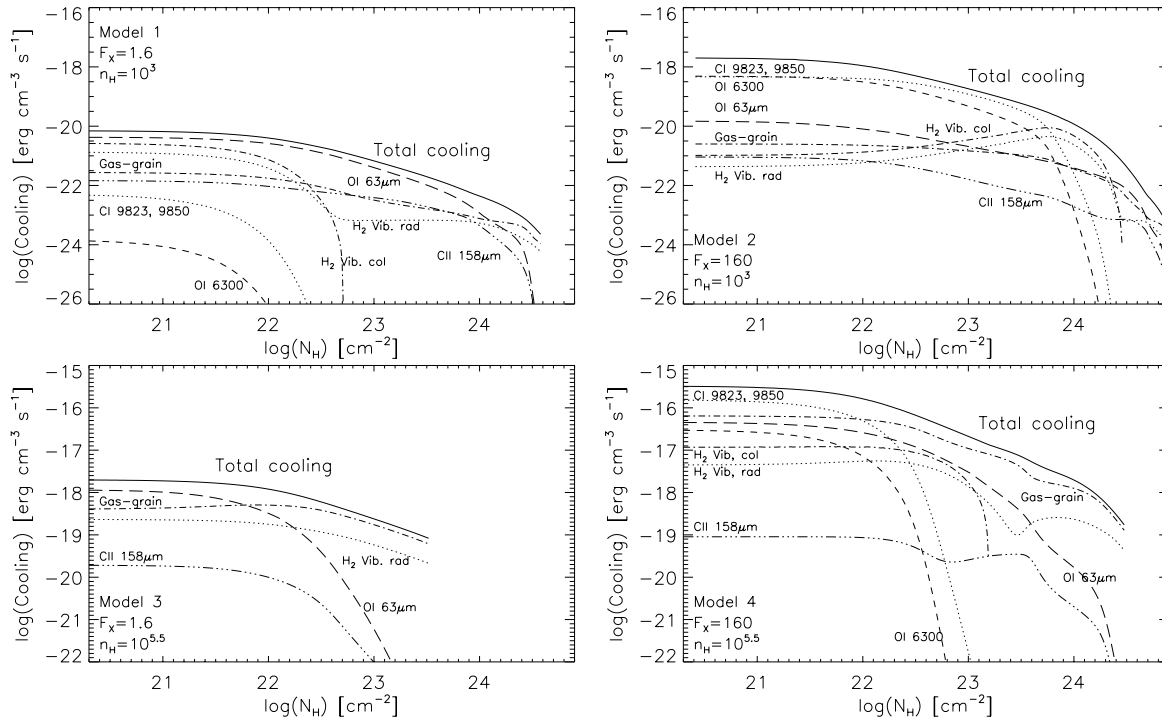
Fig. 2. Important cooling processes for Model 1 (*top left*), 2 (*top right*), 3 (*bottom left*) and 4 (*bottom right*).

dominance to occur where most of the X-rays are absorbed, but for high energy deposition rates H_X/n, the temperature is high and thermal collisions dominate the population of the vibrational levels. Non-thermal excitation is dominant at low temperature, i.e., low H_X/n.

In Fig. 2, the important cooling processes are shown as a function of total hydrogen column density, N_H. At high temperatures (see Fig. 3), cooling by [CI] 9823, 9850 Å and [OI] 6300 Å metastable lines dominates, as is the case in the models with high radiation fields, Models 2 and 4. At lower temperatures, most of the cooling is provided by the fine-structure line [OI] 63 μm (90%), e.g., at the edge in the low-radiation field Models 1 and 3. In each model, gas-grain cooling dominates for low H_X/n. In addition, specific cooling processes can be important in special cases. H_2 vibrational cooling dominates at large depths in Model 2, but in Models 1, 3 and 4 it contributes no more than 10%. H_2 vibrational cooling is split into a radiative and a collisional part. When the excitation of H_2 is dominated by non-thermal electrons, the gas is heated by collisional de-excitation of H_2.

5.2. Thermal and chemical structure

In Fig. 3, we show the temperature as a function of total hydrogen column density, N_H. Variations in radiation field strength most strongly affect the high-density models. The temperature at the edge differs a factor of 30 in the high-density case. Since X-rays penetrate much deeper into a cloud than FUV photons, high temperatures are maintained to much greater depths into the clouds. H_X/n is very important in determining the thermal balance. When H_X/n is larger, this results in a higher

temperature. Therefore, Model 2 has the largest temperature throughout the cloud. Density turns out to be important as well. Note that models 1 and 4 have similar incident H_X/n and therefore have about the same temperature throughout the cloud.

In Figs. 3 and 4, we show the fractional abundances of selected species. H_X/n is not only important in the thermal balance, but also in the chemistry. Therefore Models 1 and 4 with about the same incident H_X/n, show similar abundances. The most striking difference with the PDR models is that there is no longer a well-defined transition layer $C^+ \rightarrow C \rightarrow CO$ present. On the contrary, both C and C^+ are present throughout most of the cloud having fractional abundances of $\sim 10^{-5}-10^{-4}$. Only at very low H_X/n, which results in a low temperature, is there a partial transition to CO. The transition from atomic to molecular hydrogen is much more gradual than in the PDR models. A considerable amount of OH is present in all models at all column densities. The temperature determined by H_X/n is important. In Model 3, OH has the greatest abundance ($>10^{-6}$) at all column densities. In other models such large fractions are seen only at very high depths into the cloud. The formation of CO and H_2O is most efficient at high densities and low H_X/n. Therefore, these species have large abundances throughout the high-density, low-radiation field Model 3. In Model 4, where the radiation field is somewhat higher, CO and H_2O reach high abundances only at high N_H. At low densities, they are only formed at large depths into the cloud (Models 1 and 2). Secondary ionisations are most important for the production of H^+. Recombination is slower at lower densities. Therefore, the H^+ fractional abundance is highest in Model 4. HCN, HCO^+, HNC, C_2H, CS and SiO have much larger abundances at high temperatures than in the PDR models.
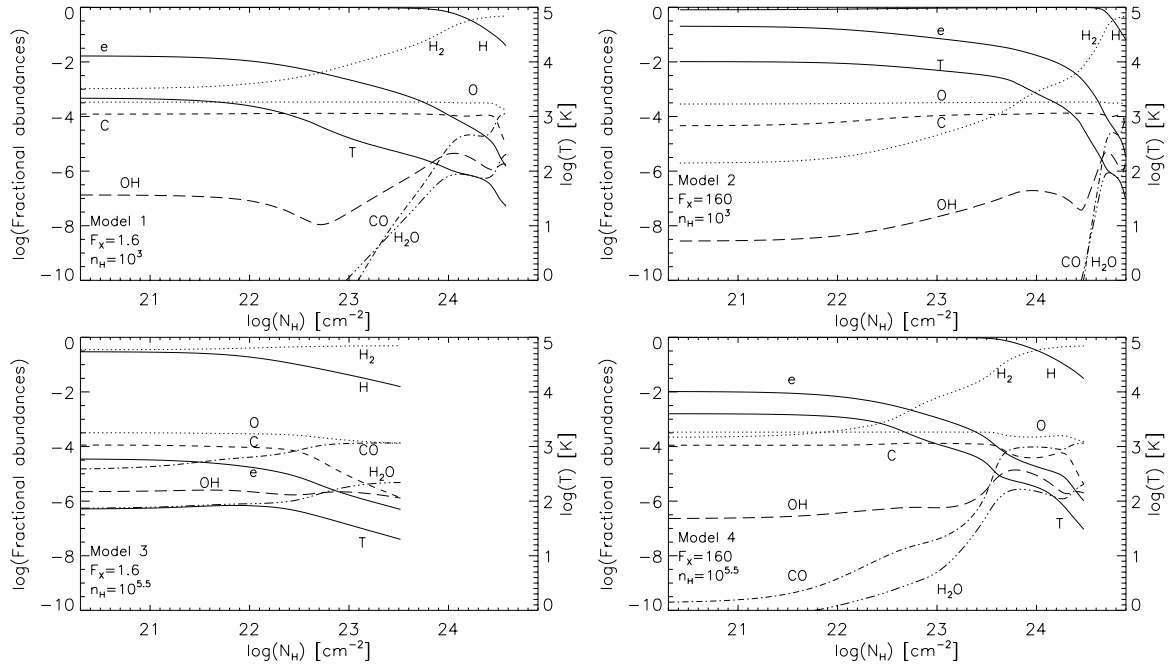
Fig. 3. Fractional abundances and temperature for Model 1 (*top left*), 2 (*top right*), 3 (*bottom left*) and 4 (*bottom right*).
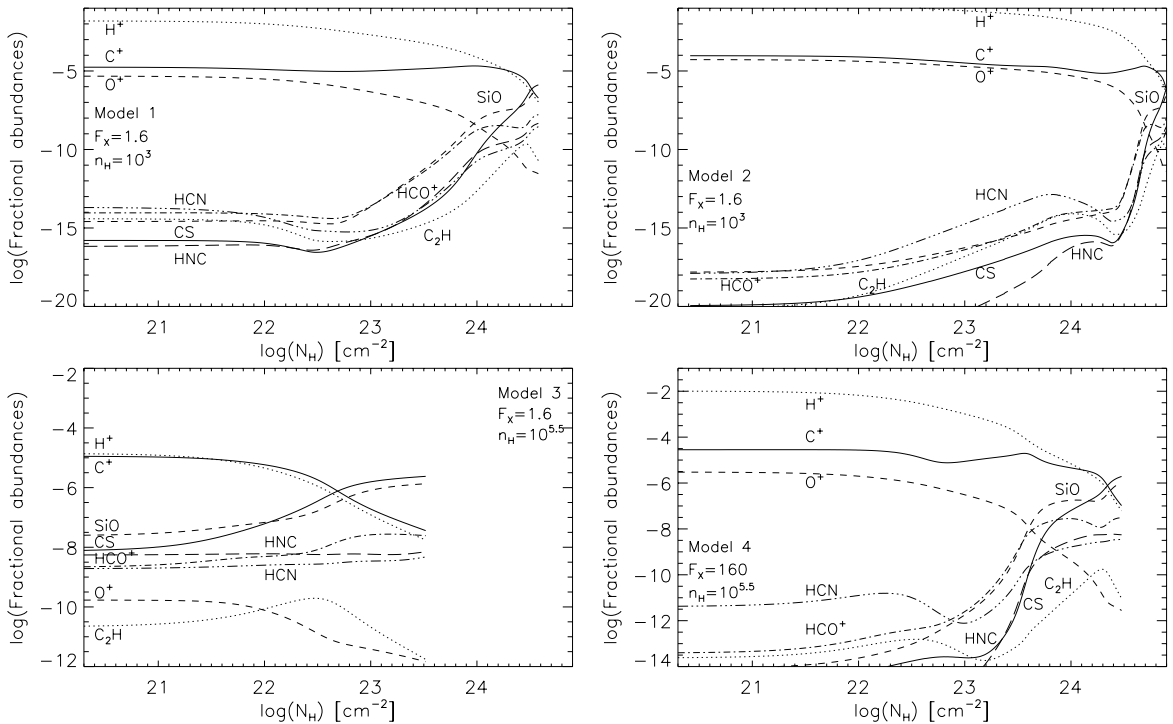

Fig. 4. Fractional abundances for model 1 (*top left*), 2 (*top right*), 3 (*bottom left*) and 4 (*bottom right*).

6. Conclusion

We now perform a direct comparison between the PDR and XDR models. To emphasise that XDRs penetrate much deeper into cloud volumes than PDRs, we use the same scale for all models. Thus, it is also possible to distinguish between gradients in abundance, cumulative intensity, column density and column density ratios. XDR Model 3 is only plotted

to $N_{\mathrm{H}} \approx 10^{23.5}$ cm^{-2}, since H_{X}/n becomes too small and no reliable results are obtained at higher column densities.

In Fig. 5, we show for Model 4 the abundances of selected species. At the edge, both neutral and ionised species are more abundant in the XDR models, and the relative abundances also differ with respect to one another. In the XDR for example, the neutral species CH and CH$_2$ are more abundant than CH$^+$ and CH$_2^+$, respectively. In the PDR, this is the other way around.
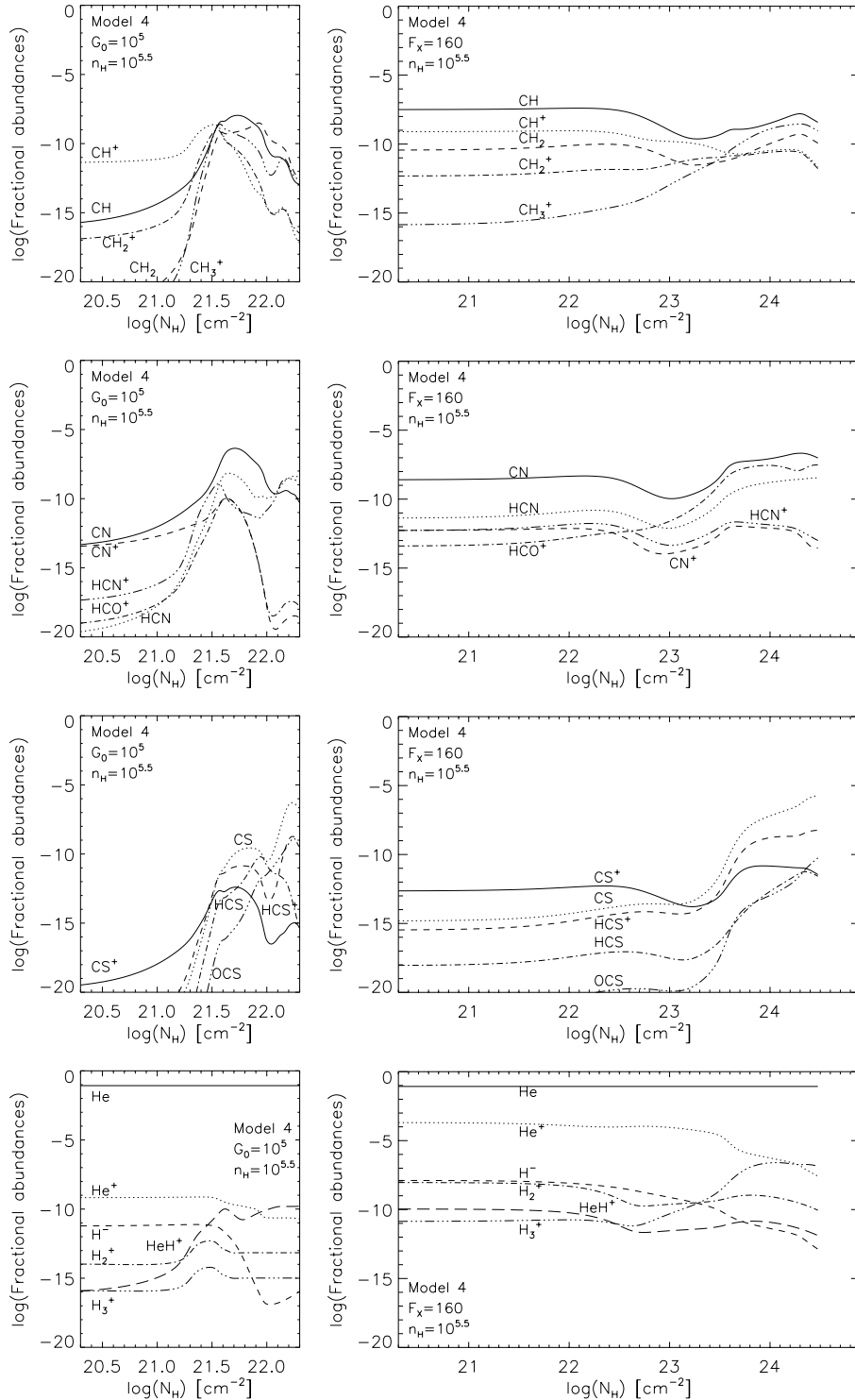
Fig. 5. Comparison between the fractional abundances in the PDR (*left*) and XDR (*right*) for Model 4.

CN and CN$^+$ are almost equally abundant at the edge in the PDR, while CN exceeds CN$^+$ by three orders of magnitude in the XDR. Although the amounts of CS$^+$ and HCS$^+$ are larger than those for CS and HCS, respectively, at the edge of the cloud in the XDR, the abundance difference is less than in the PDR. The abundance of He$^+$ is five orders of magnitude larger in the XDR, due to secondary ionisations. H$^-$ is enhanced by

three orders of magnitude, due to the higher ionisation degree. It is also easily seen that in PDRs the fractional abundances vary over many orders of magnitude, while the abundances in XDR Model 4 stay almost constant to a column density of $N_H \approx 10^{22}$ cm^{-2}, where the transition from H to H$_2$ starts.

In Figs. 6 and 7, we show cumulative line intensities for fine-structure lines at all column densities, i.e., the emergent
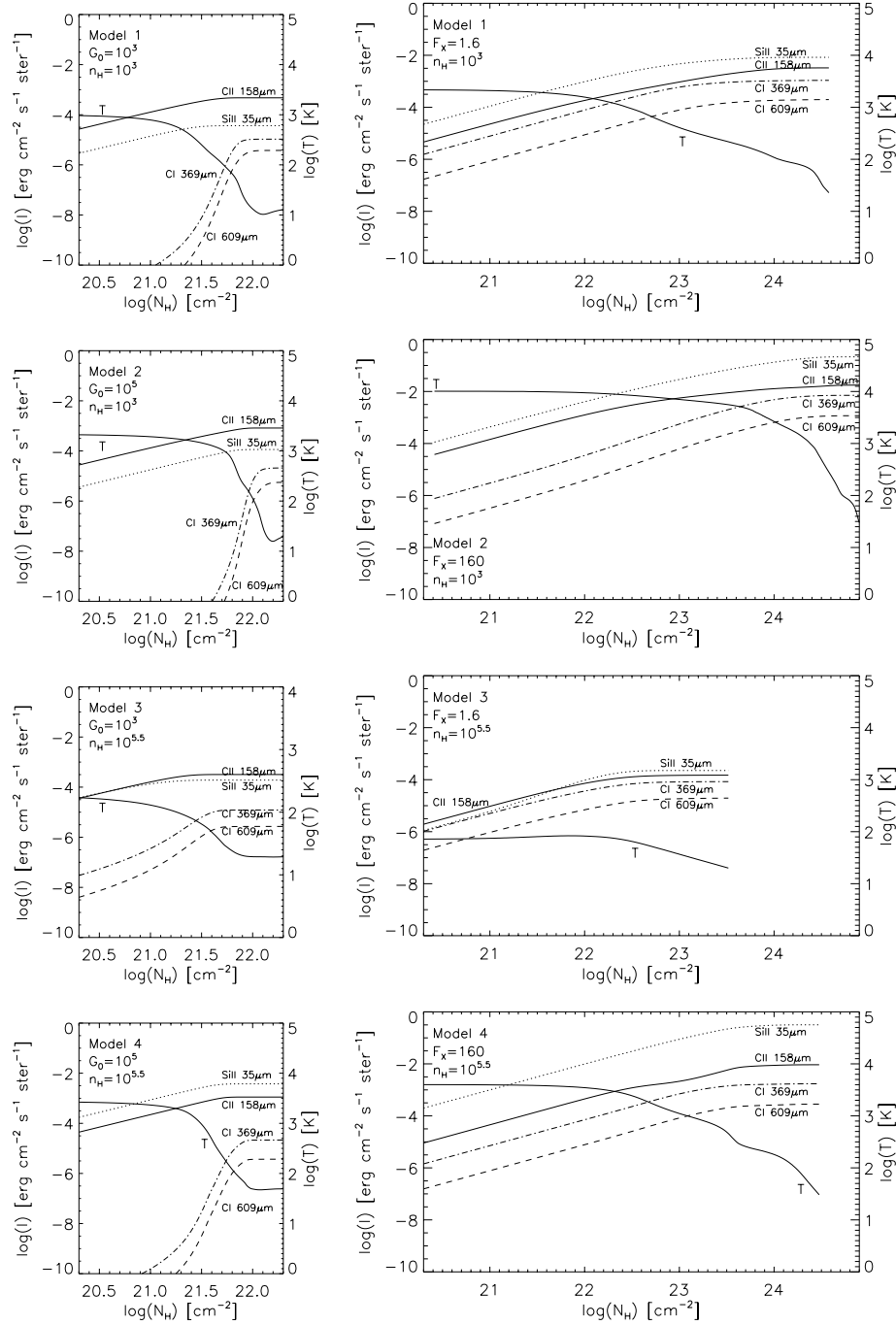
Fig. 6. Cumulative line intensities of [CII] 158 (solid), [SiII] 34.8 (dotted), [CI] 609 (dashed) and 369 μm (dashed), for PDR (*left*) and XDR (*right*) models.

intensity arising from the edge of the cloud to column density $N_{\mathrm{H}} = n_{\mathrm{H}}z$:

$$I(z) = \frac{1}{2\pi} \int_0^z \Lambda(z')\mathrm{d}z'. \qquad (1)$$

Although the total [CII] 158 μm line intensity is higher in the XDR, the flux originating from the edge to $N_{\mathrm{H}} \approx 10^{22}$ cm^{-2} is higher in the PDR except when the XDR is characterised by very high H_{X}/n values which is the case in Model 2. In

all PDR models, all carbon is in C$^+$ at the edge, while a large part of the carbon is neutral in XDR Models 1, 3 and 4. In all models, oxygen is mostly in atomic form. The [OI] 63 μm line intensity to $N_{\mathrm{H}} \approx 10^{22}$ cm^{-2} is larger in the low-density XDR models, which is possible due to higher electron abundances. The intensity is lower in the low radiation, high density XDR Model 3, since the temperature is higher in the PDR. For Model 4 they are about the same, since the density where the line becomes thermalised is almost reached. In the XDR, all line intensities increase approximately steadily with
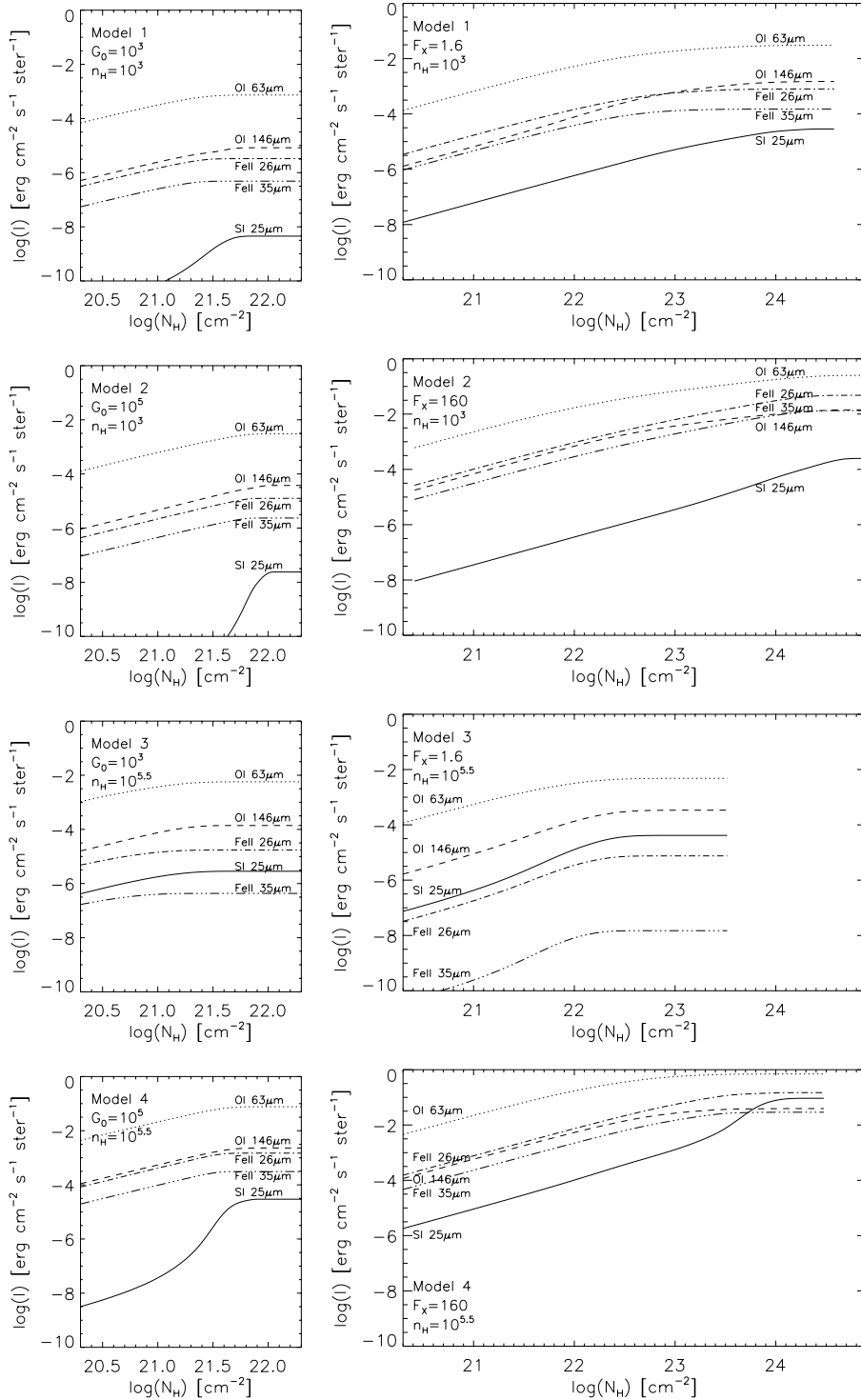
Fig. 7. Cumulative line intensities of [SI] 25.2 (solid), [OI] 63.2 (dotted), 145.6 (dashed), [FeII] 26.0 (dot-dashed) and 35.4 μm (dotted-dashed), for PDR (*left*) and XDR (*right*) models.

increasing column density. PDRs, however, primarily affect cloud surfaces causing more sudden changes. The line intensities of [CI] 609 μm and 369 μm arise from a more or less well defined part part of the cloud and start to increase at column densities $N_H \geq 10^{21.5}$ cm^{-2}. The line intensities of [CII] 158 μm are higher than those of [SiII] 35 μm in the PDRs except in Model 4. This is in contrast to the XDR models, where the

[SiII] 35 μm line intensity is always stronger. The fact that [SiII] 35 μm lines are quite strong in XDRs was already noted by Maloney et al. (1996). The line intensities for [FeII] 26 μm and 35 μm are higher for the XDR models except again for Model 3.

In Figs. 8 and 9, we show cumulative column densities for selected species. They illustrate again that XDRs affect
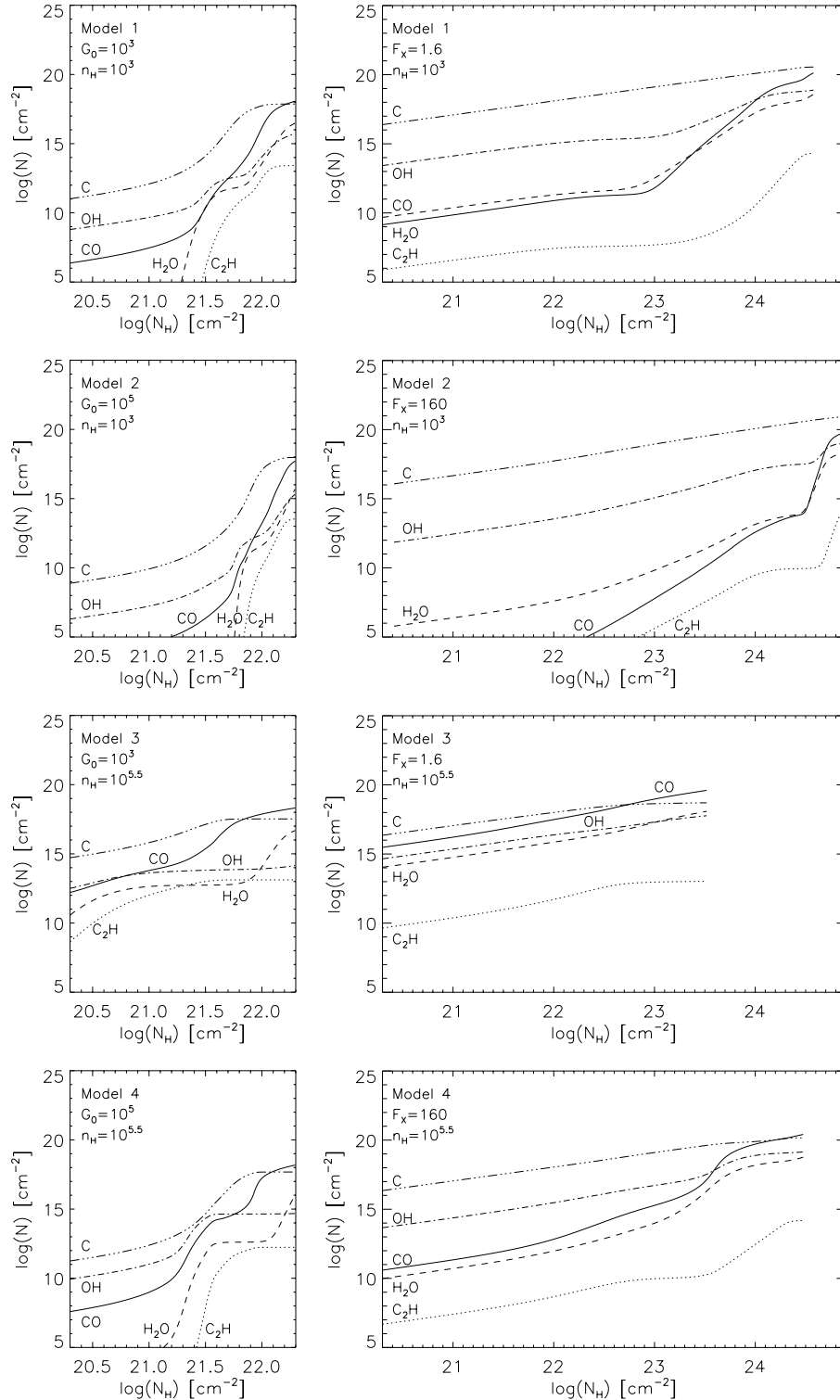
Fig. 8. Cumulative column densities of C (dotted-dashed), CO (solid), C_2H (dotted), H_2O (dashed) and OH (dot-dashed), for PDR (*left*) and XDR (*right*) models.

whole cloud volumes and PDRs create layered structures. In PDRs, the increase in column densities is very sudden for all species. For example, C and CO show this due to the very distinct C^+/C/CO transition. In the XDRs, however, the increases in column density are much more gradual. The only sudden change in XDRs is where the H/H_2 transition occurs.

In Fig. 10, the cumulative column density ratios for CO/H_2, CO/C, HNC/HCN and HCO^+/HCN are shown as a function of total hydrogen column density. The ratios for the XDRs are almost constant up to $N_H \approx 10^{22}$ cm^{-2}, unlike those in PDR models. In PDRs, CO/C ratios increase by approximately four orders of magnitude from the edge ($\leq 10^{-4}$)
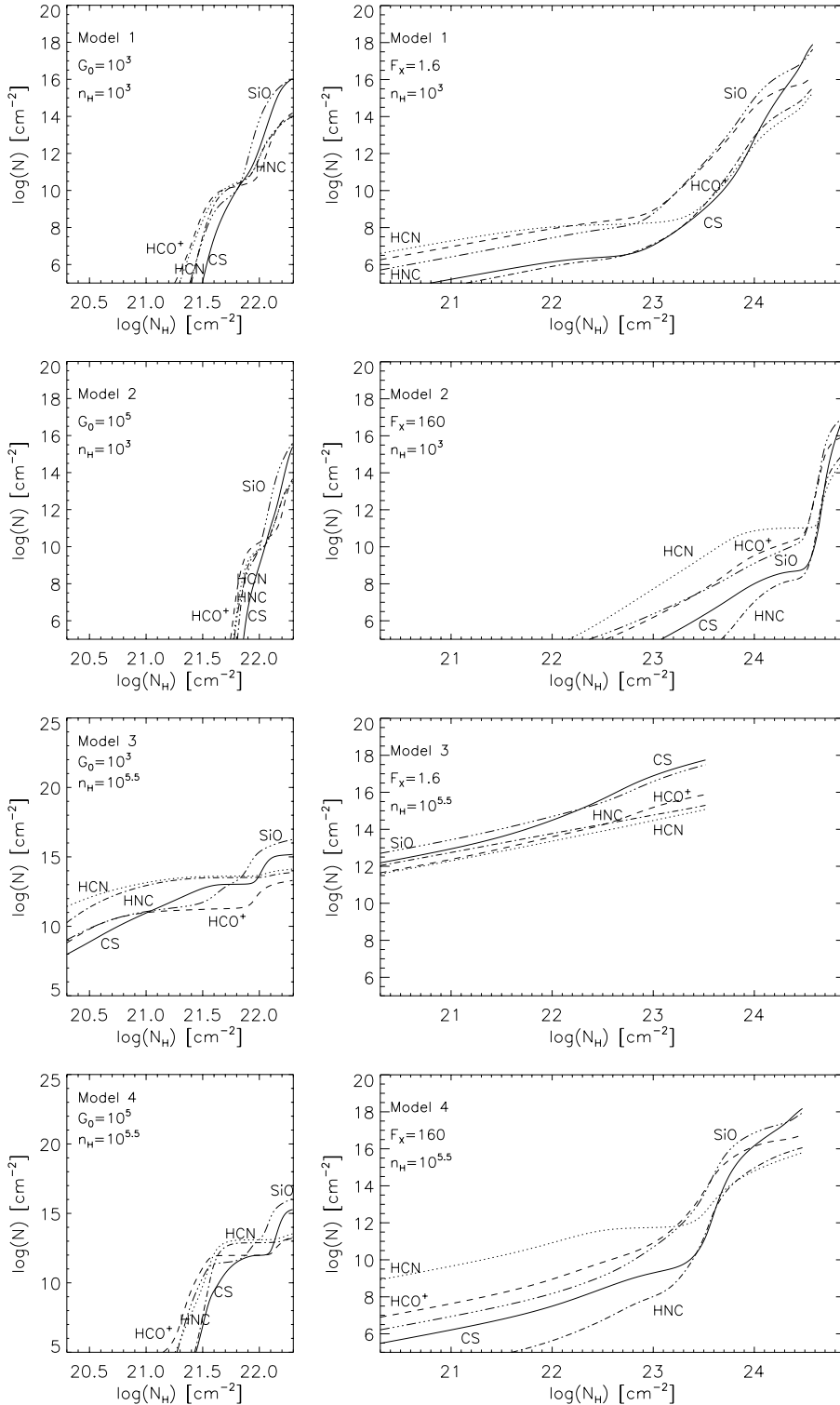
Fig. 9. Cumulative column densities of CS (solid), HCN (dotted), HCO$^+$ (dashed), HNC (dot-dashed) and SiO (dotted-dashed), for PDR (*left*) and XDR (*right*) models.

to $N_H = 10^{22.3}$ cm^{-2} (≥ 1). In XDRs, this ratio is constant to $N_H \approx 10^{22}$ cm^{-2} and then increases slowly. For each cloud size, while keeping the energy input the same, CO/C ratios increase at higher densities. The ratios go down for higher radiation fields. For the same density and energy input, CO/C is lower when the cloud is irradiated by X-ray photons, with

the exception of Model 3 where this is only valid at $N_H > 10^{21.7}$ cm^{-2}. CO/H$_2$ is somewhat more complex. When only the energy input is increased in PDRs, this ratio is higher when $N_H < 10^{21}$ cm^{-2}. For $N_H = 10^{22.3}$ cm^{-2}, the ratios are about the same. There is also a minimum where the H/H$_2$ transition occurs. This minimum is more prominent for higher radiation
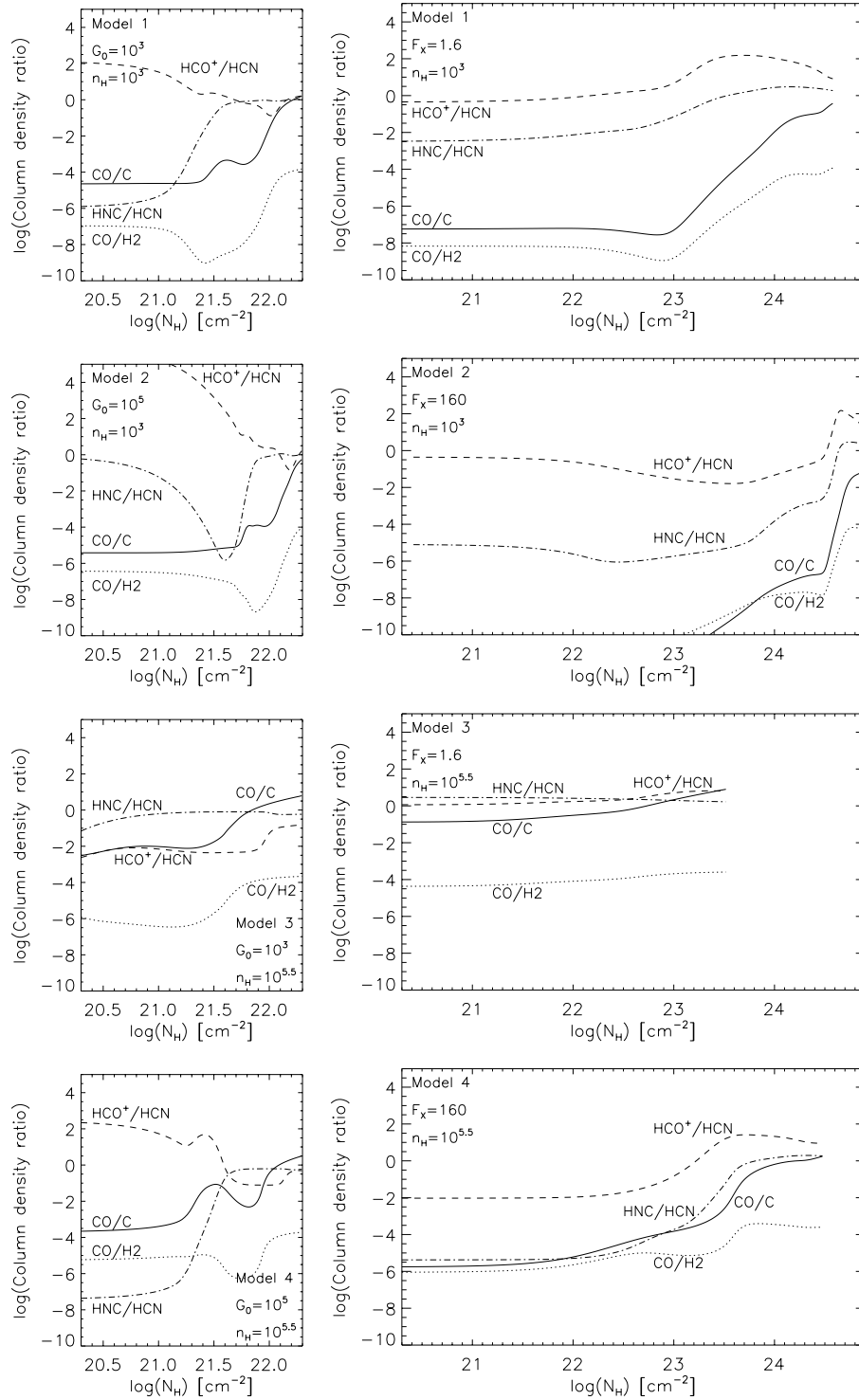
Fig. 10. Column density ratios CO/C (solid), CO/H$_2$ (dotted), HCO$^+$/HCN (dashed) and HNC/HCN (dot-dashed), for PDR (*left*) and XDR (*right*) models.

fields. In XDRs, the CO/H$_2$ ratio is lower when the radiation field is higher. In PDRs and XDRs, the CO/H$_2$ ratios are higher when the density is increased. When the cloud is irradiated by X-ray photons, CO/H$_2$ ratios are lower, again with the exception of Model 3 at $N_H < 10^{21.5}$ cm^{-2}. In PDR Models 1, 2, and 3, significant column densities for HCN, HNC and HCO$^+$ are reached between $N_H = 10^{21.5}$ and 10^{22} cm^{-2}. Therefore,

the HNC/HCN and HCO$^+$/HCN ratios discussed are for column densities $N_H > 10^{22}$ cm^{-2}. In PDRs, HNC/HCN is lower when the density is higher. No significant changes are seen for different radiation fields in these columns. HNC/HCN is generally lower for high H_X/n in XDRs. At high column densities, where H_X/n is low, HCN/HNC ratios are equal or somewhat higher than those for the PDR. HCO$^+$/HCN

and HNC/HCN are of the same order of magnitude in PDRs, but in XDRs HCO$^+$/HCN is higher in most cases.

References

Asplund, M., Grevesse, N., & Sauval, J. 2004, ArXiv Astrophysics e-prints

Bakes, E. L. O., & Tielens, A. G. G. M. 1994, ApJ, 427, 822

Bertoldi, F., & Draine, B. T. 1996, ApJ, 458, 222

Black, J. H., & Dalgarno, A. 1976, ApJ, 203, 132

Black, J. H., & Dalgarno, A. 1977, ApJS, 34, 405

Bohlin, R. C., Savage, B. D., & Drake, J. F. 1978, ApJ, 224, 132

Boland, W., & de Jong, T. 1982, ApJ, 261, 110

Cazaux, S., & Tielens, A. G. G. M. 2002, ApJ, 575, L29

Cazaux, S., & Tielens, A. G. G. M. 2004, ApJ, 604, 222

Chambaud, G., Levy, B., Millie, P., et al. 1980, J. Phys. B Atomic Molecular Phys., 13, 4205

Cravens, T. E., & Dalgarno, A. 1978, ApJ, 219, 750

Dalgarno, A., Yan, M., & Liu, W. 1999, ApJS, 125, 237

de Jong, T., Boland, W., & Dalgarno, A. 1980, A&A, 91, 68

Draine, B. T. 1978, ApJS, 36, 595

Dufton, P. L., & Kingston, A. E. 1994, Atomic Data and Nuclear Data Tables, 57, 273

Field, G. B., Goldsmith, D. W., & Habing, H. J. 1969, BAAS, 1, 240

Field, G. B., Somerville, W. B., & Dressler, K. 1966, ARA&A, 4, 207

Glassgold, A. E., & Langer, W. D. 1973, ApJ, 179, L147

Gould, R. J., & Salpeter, E. E. 1963, ApJ, 138, 393

Habing, H. J. 1969, Bull. Astron. Inst. Netherlands, 20, 177

Hollenbach, D., & McKee, C. F. 1979, ApJS, 41, 555

Hollenbach, D., & McKee, C. F. 1989, ApJ, 342, 306

Hollenbach, D., & Salpeter, E. E. 1971, ApJ, 163, 155

Hollenbach, D. J., Takahashi, T., & Tielens, A. G. G. M. 1991, ApJ, 377, 192

Jaquet, R., Staemmler, V., Smith, M. D., & Flower, D. R. 1992, J. Phys. B Atomic Molecular Phys., 25, 285

Jenkins, E. B. 2004, in Origin and Evolution of the Elements, 339

Johnson, C. T., Burke, P. G., & Kingston, A. E. 1987, J. Phys. B Atomic Molecular Phys., 20, 2553

Katz, N., Furman, I., Biham, O., Pirronello, V., & Vidali, G. 1999, ApJ, 522, 305

Kaufman, M. J., Wolfire, M. G., Hollenbach, D. J., & Luhman, M. L. 1999, ApJ, 527, 795

Le Bourlot, J., Pineau Des Forets, G., Roueff, E., & Flower, D. R. 1993, A&A, 267, 233

Le Petit, F., Roueff, E., & Le Bourlot, J. 2002, A&A, 390, 369

Le Teuff, Y. H., Millar, T. J., & Markwick, A. J. 2000, A&AS, 146, 157

Lee, H.-H., Herbst, E., Pineau des Forets, G., Roueff, E., & Le Bourlot, J. 1996, A&A, 311, 690

Lennon, M. A., Bell, K. L., Gilbody, H. B., et al. 1988, J. Phys. Chem. Reference Data, 17, 1285

Lepp, S., & Dalgarno, A. 1988, ApJ, 335, 769

Lepp, S., & Shull, J. M. 1983, ApJ, 270, 578

London, R. 1978, ApJ, 225, 405

Maloney, P. R., Hollenbach, D. J., & Tielens, A. G. G. M. 1996, ApJ, 466, 561

McLaughlin, B. M., & Bell, K. L. 1993, ApJ, 408, 753

Mendoza, C. 1983, in Planetary Nebulae, IAU Symp., 103, 143

Morrison, R., & McCammon, D. 1983, ApJ, 270, 119

Neufeld, D. A., & Kaufman, M. J. 1993, ApJ, 418, 263

Neufeld, D. A., Lepp, S., & Melnick, G. J. 1995, ApJS, 100, 132

Pirronello, V., Liu, C., Roser, J. E., & Vidali, G. 1999, A&A, 344, 681

Roueff, E., & Le Bourlot, J. 1990, A&A, 236, 515

Sampson, D. H., Zhang, H. L., & Fontes, C. J. 1994, Atomic Data and Nuclear Data Tables, 57, 97

Savage, B. D., Drake, J. F., Budich, W., & Bohlin, R. C. 1977, ApJ, 216, 291

Schröder, K., Staemmler, V., Smith, M. D., Flower, D. R., & Jaquet, R. 1991, J. Phys. B Atomic Molecular Phys., 24, 2487

Shull, J. M. 1978, ApJ, 219, 877

Spaans, M. 1996, A&A, 307, 271

Spaans, M., & Silk, J. 2000, ApJ, 538, 115

Spaans, M., Tielens, A. G. G. M., van Dishoeck, E. F., & Bakes, E. L. O. 1994, ApJ, 437, 270

Spitzer, L. J. 1978, JRASC, 72, 349

Stecher, T. P., & Williams, D. A. 1967, ApJ, 149, L29

Sternberg, A., & Dalgarno, A. 1989, ApJ, 338, 197

Sternberg, A., & Dalgarno, A. 1995, ApJS, 99, 565

Stoerzer, H., & Hollenbach, D. 1998, ApJ, 495, 853

Tielens, A. G. G. M., & Hollenbach, D. 1985, ApJ, 291, 722

Tine, S., Lepp, S., Gredel, R., & Dalgarno, A. 1997, ApJ, 481, 282

Turner, J., Kirby-Docken, K., & Dalgarno, A. 1977, ApJS, 35, 281

van Dishoeck, E. F., & Black, J. H. 1986, ApJS, 62, 109

van Dishoeck, E. F., & Black, J. H. 1988, ApJ, 334, 771

Verner, D. A., & Yakovlev, D. G. 1995, A&AS, 109, 125

Voit, G. M. 1991, ApJ, 377, 158

Wadehra, J. M., & Bardsley, J. N. 1978, Phys. Rev. Lett., 41, 1795

Weingartner, J. C., & Draine, B. T. 2001, ApJS, 134, 263

Werner, M. W. 1970, Astrophys. Lett., 6, 81

Wolfire, M. G., Hollenbach, D., & Tielens, A. G. G. M. 1993, ApJ, 402, 195

Wolfire, M. G., McKee, C. F., Hollenbach, D., & Tielens, A. G. G. M. 2003, ApJ, 587, 278

Yan, M. 1997, Ph.D. Thesis, Center for Astrophysics, Harvard University

Online Material

Appendix A: Heating processes in PDRs

A.1. Photo-electric emission

In PDRs the photo-electric emission from (small) dust grains and PAHs is the dominant heating source. We use the analytical expression given by Bakes & Tielens (1994) which is given by

$$\Gamma_{\text{grain}} = 10^{-24} \epsilon\, G'_{0,\text{dust}}\, n_{\text{H}} \text{ erg cm}^{-3} \text{ s}^{-1}, \tag{A.1}$$

where $G'_{0,\text{dust}}$ is the radiation field attenuated by dust absorption (Black & Dalgarno 1977) and the heating efficiency ϵ is given by

$$\epsilon = \frac{4.87 \times 10^{-2}}{\left[1 + 4 \times 10^{-3}(G_0 T_{\text{k}}^{1/2}/n_{\text{e}})^{0.73}\right]}$$
$$+ \frac{3.65 \times 10^{-2}(T_{\text{k}}/10^4)^{0.7}}{\left[1 + 2 \times 10^{-4}(G_0 T_{\text{k}}^{1/2}/n_{\text{e}})\right]}. \tag{A.2}$$

Note that the efficiency depends on the ratio $G_0\, T_{\text{k}}^{1/2}/n_{\text{e}}$, which is the ratio of the ionisation and recombination rates. A_{V} is the visual extinction at optical wavelengths caused by interstellar dust. Bohlin et al. (1978) relate the total column density of hydrogen, $N_{\text{H}} = N(\text{H}) + 2N(\text{H}_2)$ to colour excess, $E(B - V)$:

$$\frac{N_{\text{H}}}{E(B - V)} = 5.8 \times 10^{21} \text{ cm}^{-2} \text{ mag}^{-1}. \tag{A.3}$$

The visual extinction then follows consequently: $A_{\text{V}} = 3.1E(B - V)$ and $A_{\text{V}} = 5.34 \times 10^{-22}N_{\text{H}}$. Note that the results of Savage et al. (1977) are often used, but in this paper only H_2 (and not H I) is taken into account.

A.2. Carbon ionisation heating

At the edge of the cloud, most of the carbon is singly ionised. The photo-electron energy released in an ionisation is $\Delta E_{\text{C}} = 1.06$ eV. The ionisation rate, at a certain point in the cloud, is given by $\kappa_{\text{ion}} = 1.76 G'_{0,\text{carbon}}$ s^{-1}. The heating rate due to the ionisation of carbon is then given by

$$\Gamma_{\text{C}} = \kappa_{\text{ion}}\, n(\text{C})\, \Delta E_{\text{C}}. \tag{A.4}$$

After substitution of numerical values we get the following heating rate for the local radiation field $G'_{0,\text{carbon}}$:

$$\Gamma_{\text{C}} = 2.79 \times 10^{-22}\, n(\text{C})\, G'_{0,\text{carbon}} \text{ erg cm}^{-3} \text{ s}^{-1}, \tag{A.5}$$

where this time $G'_{0,\text{carbon}}$ is the radiation field attenuated by dust absorption (Black & Dalgarno 1977), carbon self-absorption (Werner 1970) and H_2 (de Jong et al. 1980).

A.3. H_2 photo-dissociation heating

Absorption of Lyman-Werner band photons leads to the excitation of H_2. About 10% of the excitations leads to decay into the continuum of the ground electronic state (Field et al. 1966; Stecher & Williams 1967). The heating related to this dissociation is given by

$$\Gamma = 0.1\, \kappa_{\text{exc.}} \langle E_{\text{diss}} \rangle, \tag{A.6}$$

where $\langle E_{\text{diss}} \rangle$ is the mean kinetic energy of the H atoms and is set to 0.4 eV (Spaans 1996). The excitation rate of H_2 is given by $\kappa_{\text{exc.}} = 3.4 \times 10^{-10}\, G'_{0,\text{H}_2}$, where G'_{0,H_2} is the local radiation field given by

$$G'_{0,\text{H}_2} = \beta(\tau)G_0 \exp(-2.5\, A_{\text{V}}). \tag{A.7}$$

Self-shielding is explicitly taken into account for the excitation of H_2, by the introduction of the shielding factor $\beta(\tau)$ (see Sect. D.2.3). After substitution of numerical values we get a heating rate of

$$\Gamma_{\text{H}_2} = 2.2 \times 10^{-23}\, \beta(\tau)\, G_0 \tag{A.8}$$
$$\exp(-2.5\, A_{\text{V}}) \text{ erg cm}^{-3} \text{ s}^{-1}.$$

A.4. H_2 collisional de-excitation heating

FUV excitation is followed by decay to ro-vibrational levels in the ground state. Collisional de-excitation leads to gas heating. This cascade process is very complicated, but we simplify this process by using a two-level approximation (see Sect. D.2.2). The resulting heating rate is given by

$$\Gamma_{\text{H}_2} = \left[n(\text{H})\gamma_{10}^{\text{H}} + n(\text{H}_2)\gamma_{10}^{\text{H}_2}\right] n(\text{H}_2\text{V})E_* \text{ erg cm}^{-3} \text{ s}^{-1}, \tag{A.9}$$

where the coefficients are given by Hollenbach & McKee (1979)

$$\gamma_{10}^{\text{H}} = 10^{-12}\, T_{\text{k}}^{0.5}\exp(-1000/T_{\text{k}}) \tag{A.10}$$
$$\gamma_{10}^{\text{H}_2} = 1.4 \times 10^{-12}T_{\text{k}}^{0.5}\exp(-18\,100/(T_{\text{k}} + 1200)). \tag{A.11}$$

Both of the above expression are in units of cm^3 s^{-1}.

A.5. Gas-grain collisional heating

When gas and grains differ in temperature they can transfer heat through collisions. The heating rate of the gas is given by (Hollenbach & McKee 1979, 1989)

$$\Gamma_{\text{coll.}} = 1.2 \times 10^{-31}n^2 \left(\frac{T_{\text{k}}}{1000}\right)^{1/2} \left(\frac{100 \text{ Å}}{a_{\text{min}}}\right)^{1/2} \tag{A.12}$$
$$\times[1 - 0.8\exp(-75/T_{\text{k}})](T_{\text{d}} - T_{\text{k}}).$$

The minimum grain size is set at $a_{\text{min}} = 10$ Å and the dust temperature T_{d} is given by

$$T_{\text{d}} = \big(8.9 \times 10^{-11}\nu_0 G_0 \exp(-1.8A_{\text{V}}) \tag{A.13}$$
$$+2.7^5 + 3.4 \times 10^{-2}\left[0.42 - \ln(3.5 \times 10^{-2}\tau_{100}T_0)\right]$$
$$\times\tau_{100}T_0^6\big)^{0.2},$$

based on the results of Hollenbach et al. (1991).

A.6. Gas-grain viscous heating

Radiation pressure accelerates grains relative to the gas and the resulting drag contributes viscous heating to the gas. Grain acceleration time scales are short compared to other time scales, and therefore the grains may be considered moving at their local drift velocity, v_{d}. All the momentum is transferred to

the gas, predominantly by Coulomb forces. For drift velocities $v_d < 10^3$ cm s^{-1} (Spitzer 1978), no significant gas-grain separation takes place. In the following we take $v_d = 10^2$ cm s^{-1}. The heating rate is given by

$$\Gamma_{\text{visc.}} = 8\pi e^4 n_d Z_d^2 (kT_k)^{-1}(\ln \Lambda) v_d$$
$$[n(C^+)G(y_{C^+}) + n_e G(y_e)], \qquad (A.14)$$

where n_d is the grain volume density, Z_d is the grain charge, $n(C^+)$ and n_e are the respective C^+ and electron volume densities and the functions Λ and $G(y)$ are given by

$$\Lambda = 1.5 Z_d^{-1} e^{-3}(kT_k)^{1.5}(\pi n_e)^{-0.5} \qquad (A.15)$$
$$G(y) = \frac{1}{2y^2}\left\{ \text{erf}(y) - \frac{2}{\pi^{0.5}}ye^{-y^2} \right\}, \qquad (A.16)$$

where $y = v_d/v_{\text{th}}$ and v_{th} the thermal velocity of C^+ ions and electrons. The error function erf(y) is given by

$$\text{erf}(y) = \int_0^y e^{-t^2} dt. \qquad (A.17)$$

A.7. Cosmic-ray heating

At large column densities, cosmic ray heating can become important. Glassgold & Langer (1973) and Cravens & Dalgarno (1978) calculated that the amount of heat deposited in a molecular gas is about 8 keV per primary ionisation. Then, Tielens & Hollenbach (1985) find for the total heating rate, including helium ionisation

$$\Gamma_{\text{CR}} = 1.5 \times 10^{-11} \zeta\, n(H_2) \text{ erg cm}^{-3} \text{ s}^{-1}, \qquad (A.18)$$

where ζ is the cosmic ray ionisation rate per H_2 molecule.

Appendix B: Heating processes in XDRs

B.1. Heating due to Coulomb interactions

When X-rays are absorbed, fast electrons are produced. These fast electrons lose part of their energy through Coulomb interactions with thermal electrons, so the X-ray heating is given by

$$\Gamma_X = \eta\, n\, H_X, \qquad (B.1)$$

where η is the heating efficiency, depending on the H_2/H ratio and the electron abundance x. We use the results of Dalgarno et al. (1999). Their calculated heating efficiency η in an ionised gas mixture is given by

$$\eta = \frac{10r\eta_{H_2He} + \eta_{HeH}}{10r + 1}, \qquad (B.2)$$

where $r = n(H_2)/n(H)$. η_{H_2H} and η_{HeH} are the heating efficiencies for the ionised pure He and H_2 mixture and the He and H mixture, respectively. Both are parametrised through

$$\eta' = 1 + (\eta_0 - 1)/(1 + cx^\alpha). \qquad (B.3)$$

The values of η_0, c and α are given in Table 7 of Dalgarno et al. (1999), and x is the electron fractional abundance. It has to be modified when the H_2-He mixture is considered:

$$x' = \frac{1.83x}{1 + 0.83x}. \qquad (B.4)$$

B.2. Heating due to H_2 ionisation

H_2 ionisation can lead to gas heating (Glassgold & Langer 1973). When H_2 is ionised by a fast electron and subsequently recombines dissociatively, about 10.9 eV (1.75×10^{-11} erg) of the ionisation energy can go into kinetic energy. H_2^+ can also charge transfer with H. This is an exothermic reaction, with an energy yield of 1.88 eV, of which we assume half, 0.94 eV (1.51×10^{-12} erg), to go into heating. H_2^+ can also react to H_3^+, and subsequently recombine dissociatively or react with other species. Glassgold & Langer (1973) argued that for every H_3^+ ion formed 8.6 eV (1.37×10^{-11} erg) goes into gas heating. The H_2 ionisation rate cooling is then given by

$$\Gamma_{H_2 \text{ ion}} = \frac{17.5k_e x_e + 1.51k_H x_H + 13.7k_{H_2}x_{H_2}}{k_e x_e + k_H x_H + k_{H_2}x_{H_2}} \qquad (B.5)$$
$$\times 10^{-12}\zeta_{H_2}\, x_{H_2}\, n \text{ erg cm}^{-3}\text{s}^{-1},$$

where k_e, k_H and k_{H_2} are the rates of dissociative recombination, charge transfer with hydrogen and the reaction to H_3^+, respectively.

B.3. Gas-grain collisional heating

We use the results of Sect. A.5. The dust temperature was found by Yan (1997):

$$T_d = 1.5 \times 10^4 (H_X/x_d)^{0.2} \text{ K}, \qquad (B.6)$$

where $x_d = 1.6 \times 10^{-8}$ is the grain abundance and H_X in erg s^{-1}.

B.4. H_2 vibrational heating/cooling

When the vibrational levels of H_2 are populated by non-thermal processes, thermal collisional quenching and excitation can result in a net heating despite downward radiations. When non-thermal reactions are not important, H_2 can be an important coolant. The resulting collisional vibrational heating or cooling is given by

$$\Gamma_{H_2\text{vib,col}} = \Sigma_{vj}n_{vj} \qquad (B.7)$$
$$\times\Sigma_{v'j'}C(vj \rightarrow v'j')$$
$$\times(E_{vj} - E_{v'j'}) \text{ erg cm}^{-3}\text{ s}^{-1}.$$

Where $C(vj \rightarrow v'j')$ is the total collision rate from level vj to $v'j'$ in units of s^{-1}. Radiative cooling due to downward decay of the vibrational levels is given by

$$\Lambda_{H_2\text{vib,rad}} = \Sigma_{vj}A(vj \rightarrow v'j')n_{vj} \text{ erg cm}^{-3}\text{ s}^{-1}. \qquad (B.8)$$

The population of the vibrational levels is discussed in Sect. D.3.4.

Appendix C: Cooling processes

C.1. Fine-structure line cooling

Since most of the gas is atomic in the radical region, the dominant coolants are the atomic fine-structure lines. The most prominent cooling lines are the [CII] 158 μm and [OI] 63 μm and 146 μm lines. For the calculation of the thermal balance

we also take into account Si^+, C, Si, S, Fe and Fe^+. We use a compilation for the collisional data from Sternberg & Dalgarno (1995), Hollenbach & McKee (1989), Sampson et al. (1994), Dufton & Kingston (1994), Johnson et al. (1987), Roueff & Le Bourlot (1990), Schröder et al. (1991), Mendoza (1983), Chambaud et al. (1980) and Jaquet et al. (1992). We take into account collisions with electrons, H^+, H and H_2 (ortho and para) for the excitation of the species to different levels. In the PDRs, collisions with H^+ are not the dominant excitation source but in XDRs the ionised fraction of hydrogen can be as large as ten percent and become important for the excitation of some levels.

C.2. Metastable-line cooling

We included the metastable cooling lines of C, C^+, Si, Si^+, O, O^+, S, S^+, Fe and Fe^+. All the data is taken from Hollenbach & McKee (1989) except for Si^+ (Dufton & Kingston 1994), C^+ (Sampson et al. 1994) and O^+ (McLaughlin & Bell 1993).

C.3. Recombination cooling

At temperatures higher than ~ 5000 K, cooling due to recombination of electrons with grains (PAHs) is important. The cooling depends on the recombination rate which is proportional to the product $n_e\, n_H$. The cooling rate increases when $G_0 T_k^{0.5}/n_e$ goes up, due to an increase in charge and hence Coulomb interaction. Bakes & Tielens (1994) calculated numerically the recombination cooling for a variety of physical conditions. An analytical fit to the data is given by

$$\Lambda = 3.49 \times 10^{-30} T_k^{\alpha} (G_0 T_k^{1/2}/n_e)^{\beta} \tag{C.1}$$
$$n_e n_H \text{ erg s}^{-1} \text{ cm}^{-3}$$

where $\alpha = 0.944$ and $\beta = 0.735/T_k^{0.068}$.

C.4. Molecular cooling by H_2, CO and H_2O

For the rotational and vibrational cooling of H_2, CO and H_2O, we use the fitted rate coefficients of Neufeld & Kaufman (1993) and Neufeld et al. (1995). They present a cooling rate for species i through:

$$\Lambda = L\, n(x_i)\, n(H_2) \text{ erg cm}^{-3} \text{ s}^{-1}, \tag{C.2}$$

where $n(H_2)$ and $n(x_i)$ are the densities of H_2 and species x_i, respectively. L is given by

$$\frac{1}{L} = \frac{1}{L_0} + \frac{n(H_2)}{L_{LTE}} + \frac{1}{L_0}\left[\frac{n(H_2)}{n_{1/2}}\right]^{\alpha}\left(1 - \frac{n_{1/2}}{L_{LTE}}\right). \tag{C.3}$$

We interpolate in the tables given by Neufeld & Kaufman (1993) and Neufeld et al. (1995), to find the values L_0, $n_{1/2}$ and L_{LTE} and α. L_0 is the cooling rate coefficient in the low density limit and $n_{1/2}$ is the H_2 density where L has fallen by a factor of two below L_0. α is chosen to minimize the maximal fractional error in the fit at other densities. L_0 is a function of temperature, and L_{LTE}, $n_{1/2}$, and α are functions of temperature and the optical depth parameter $\tilde{N}(x_i)$, which is given by the gradient $N(x_i)/\delta v_d$. $N(x_i)$ is the column density

of the species x_i. To take into account collisional excitation by electrons and atomic hydrogen, we follow Yan (1997) and replace $n(H_2)$ by n_{rot} and n_{vib}. For H_2 rotational and vibrational cooling, n_{rot} and n_{vib} are given by

$$n_{rot}(H_2) = n_{vib}(H_2) = n(H_2) + 7n(H) + 16n(e). \tag{C.4}$$

For rotational cooling by CO, n_{rot} is given by

$$n_{rot}(CO) = n(H_2) + 1.414 n(H)\sigma_H/\sigma_{H_2} \tag{C.5}$$
$$+ 1.3 \times 10^{-8} n(e)/\sigma_{H_2} v,$$

where $\sigma_H = 2.3 \times 10^{-15}$ cm^{-2}, $\sigma_{H_2} = 3.3 \times 10^{-16}(T_k/10^3))^{-1/4}$ cm^{-2} and $v = 1.03 \times 10^4 T_k^{0.5}$ cm s^{-1}. For H_2O rotational cooling, n_{rot} is given by

$$n_{rot}(H_2O) = n(H_2) + 10n(H) \tag{C.6}$$
$$+ n(e)k_e(1, 20, 1.9, T_k)/k_{H_2},$$

where $k_{H_2} = 7.4 \times 10^{-12} T_k^{0.5}$ cm^3 s^{-1} and $k_e(i, b, d, T_k)$ are the H_2 and electron impact excitation rate coefficients, respectively. $k_e(i, b, d, T_k)$ for the excitation from level $i \rightarrow i + 1$ in units of cm^3 s^{-1} is given by

$$k_e(i, b, d, T_k) = \frac{3.56 \times 10^{-6} d^2}{T_k^{0.5}[2 - 1/(i+1)]} \exp(\beta \Delta E) \tag{C.7}$$
$$\times \ln\left[C\Delta E + \frac{C}{\beta} \exp\left(\frac{-0.577}{1 + 2\beta\Delta E}\right)\right]$$

where b is the rotational constant in cm^{-1}, d the dipole moment in Debye, $\beta = 11\,600/T_k$, $\Delta E = 2.48 \times 10^{-4} b(i+1)$ and C is given by

$$C = \frac{9.08 \times 10^3}{b(i+1)} \qquad d \leq 1.53 \tag{C.8}$$
$$C = \frac{1.93 \times 10^4}{db(i+1)} \exp(-1.18/d^3) \qquad d > 1.53.$$

For CO vibrational cooling, n_{vib} is given by

$$n_{vib}(CO) = n(H_2) + 50n(H) + n(e)L_{CO,e}/L_{CO,0} \tag{C.9}$$

where

$$L_{CO,e} = 1.03 \times 10^{-10}(T_k/300)^{0.938} \exp(-3080/T_k) \tag{C.10}$$
$$L_{CO,0} = 1.14 \times 10^{-14} \exp(-68.0/T_k^{1/3}) \exp(-3080/T_k).$$

For H_2O vibrational cooling, n_{vib} is given by

$$n_{vib}(H_2O) = n(H_2) + 10n(H) + n(e)L_{H_2O,e}/L_{H_2O,0} \tag{C.11}$$

where

$$L_{H_2O,e} = 2.6 \times 10^{-6} T_k^{-0.5} \exp(-2325/T_k) \tag{C.12}$$
$$L_{H_2O,0} = 0.64 \times 10^{-14} \exp(-47.5/T_k^{1/3}) \exp(-2325/T_k)$$

In the XDR models, H_2 vibrational cooling is treated differently, since non-thermal processes play an important role, which is discussed in Sect. B.4.

C.5. Cooling by electron impact with H

The cooling due to the excitation of hydrogen is important at temperatures $T > 5000$ K. The cooling rate is given by Spitzer (1978):

$$\Lambda_{e-H} = 7.3 \times 10^{-19} n_e \, n(H) \qquad (C.13)$$
$$\times \exp(-118\,400/T_k) \text{ erg cm}^{-3} \text{ s}^{-1}.$$

Appendix D: Chemistry

For most of the chemical reaction rates, we make use of the UMIST database for astrochemistry by Le Teuff et al. (2000). In de PDR model we use a network containing all the species with a size up to 6 atoms. For the XDR model we use all species with sizes up to 3 atoms and some of 4 atoms. These species are taken from Yan (1997). Below we discuss the additional reactions.

D.1. H_2 formation on dust grains

The formation of H_2 is very efficient over a wide range of temperatures. It was already shown by Gould & Salpeter (1963) that H_2 is not formed efficiently in the gas phase. Most of the formation, which is still not very well understood, takes place on grain surfaces (Hollenbach & Salpeter 1971). Recently, Cazaux & Tielens (2002, 2004) developed a model for the formation of hydrogen under astrophysically relevant conditions. They compared their results with the laboratory experiments by Pirronello et al. (1999) and Katz et al. (1999). They find a recombination rate of

$$R_{H_2} = 0.5 \, n_H \, v_H \, n_d \, \sigma_d \, \epsilon_{H_2} S_H(T_k) \qquad (D.1)$$
$$\approx 6 \times 10^{-17} \, (T_k/300)^{0.5} n_H \, n \, \epsilon_{H_2} S(T_k) \text{ cm}^{-3} \text{ s}^{-1},$$

where n_d and σ_d are the volume density and cross section of dust grains and n_H, v_H and $S(T_k)$ are the volume density, thermal velocity and thermally averaged sticking coefficient of hydrogen atoms. We use the sticking coefficient given by Hollenbach & McKee (1979)

$$S(T_k) = \left[1 + 0.4(T_k + T_d)^{0.5} + 2 \times 10^{-3} \, T_k \right. \qquad (D.2)$$
$$\left. + 8 \times 10^{-6} \, T_k^2 \right]^{-1},$$

where T_d is the dust temperature. Equation (D.2) is the same as Eq. (4) in Tielens & Hollenbach (1985), except for the term ϵ_{H_2}, the recombination efficiency, which is given by

$$\epsilon_{H_2} = \left(\frac{\mu F}{2\beta_{H_2}} + 1 + \frac{\beta_{H_p}}{\alpha_{pc}}\right)^{-1}, \qquad (D.3)$$

where μ is the H_2 fraction that stays on the surface after formation, β_{H_2} and β_{H_p} are the desorption rates of molecular hydrogen and physisorbed hydrogen atoms, respectively, F is the flux of hydrogen atoms and α_{pc} is the evaporation rate from physisorbed to chemisorbed sites. These three terms dominate in different temperature regimes. See Cazaux & Tielens (2002, 2004) for a more detailed discussion.

## D.2. Additional reactions in PDR models

D.2.1. Recombination on PAHs

Collisions of electrons and ions with grains can become an important recombination process in dense clouds of low ionisation. We include reactions with PAHs following Sect. 5 of Wolfire et al. (2003) in the PDR models. The C^+/C transition occurs at larger column densities when PAHs are included. Deep into the cloud, the electron abundance is reduced by several orders of magnitude.

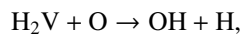### D.2.2. Vibrational excitation of H_2

In PDRs, molecular hydrogen can be excited by absorption of FUV photons in the Lyman-Werner bands. Fluorescence leads to dissociation in about 10% in of the cases (see Field et al. 1966; Stecher & Williams 1967), and in the remaining 90% of the cases to a vibrationally excited state of the ground electronic state (Black & Dalgarno 1976). To simplify matters, we treat the electronic ground state as having a vibrational ground state and a single excited vibrational state. London (1978) found that the effective quantum number for this pseudo-level is $v = 6$, and the effective energy is $E_*/k = 2.6$ eV/k = 30 163 K. We treat excited molecular hydrogen, H_2V, as a separate species in our chemistry. H_2V can be destroyed by direct FUV dissociation, radiative decay or collisional de-excitation, and chemical reactions with other species. Since vibrational decay is a forbidden process, a large abundance of H_2V can be maintained. H_2V can react with other species with no activation barrier or a reduced one. In the UMIST database, the rates for a reaction between two species are parameterised as

$$R = \alpha \, (T_k/300)^\beta \, \exp(-\gamma /T_k) \text{ cm}^3 \text{ s}^{-1}. \qquad (D.4)$$

For reactions with H_2V, γ is replaced by $\gamma^* = \max(0.0, \gamma - 30\,163)$. When reactions have an activation barrier lower than 2.6 eV, the barrier is set to zero. When the barrier is larger than 2.6 eV, the barrier is reduced by 2.6 eV. Tielens & Hollenbach (1985) state that for important reactions such as

$$H_2V + C^+ \rightarrow CH^+ + H$$

and

$$H_2V + O \rightarrow OH + H,$$
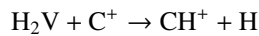
this is a good approximation since the activation barrier of ~0.5 eV is a lot smaller than the vibrational excitation energy of 2.6 eV. For reactions with barriers of the same order or larger one can overestimate the reaction rates.

D.2.3. Shielding of H_2 and CO

In PDRs, the photo-dissociation rate of both H_2 and CO is influenced by line as well as continuum absorption. The dissociation rate of H_2 is decreased by self-shielding. For an H_2 line optical depth $\tau \leq 10$, we adopt the self-shielding factor given by (Shull 1978). When the line absorption is dominated by the Doppler cores or the Lorentz wings (i.e., $\tau > 10$), we use the self-shielding factor as given by de Jong et al. (1980).

The CO photo-dissociation rate is decreased by both CO self-shielding and H_2 mutual shielding. We use Table 5 of van Dishoeck & Black (1988), to determine the shielding factor as a function of column densities $N(H_2)$ and $N(CO)$.

D.3. Additional reactions in XDRs

D.3.1. Primary ionisations

In the XDRs we do not use the photo-ionisation rates from UMIST. X-rays are absorbed in K-shell levels releasing an electron. An electron from a higher level may fill the empty spot and with the energy surplus another so called Auger electron is ejected. This process leads to multiply ionised species. Due to charge transfer with H, H_2 and He, they are quickly reduced to the doubly ionised state. We therefore assume that the ionisation by an X-ray photon leads to a doubly ionised species, as does absorption of an X-ray photon by a singly ionised species. When rates for charge transfer with H and He are very fast, elements are quickly reduced to singly ionised atoms, which is the case for O^{2+}, Si^{2+} and Cl^{2+}. Therefore, we add only O^{2+} to the chemical network to represent them. We assume that Si and Cl get singly ionised after absorbing an X-ray photon. We also include C^{2+}, N^{2+}, S^{2+} and Fe^{2+}. The direct (or primary) ionisation rate of species i at a certain depth z into the cloud is given by

$$\zeta_{i,\mathrm{prim}} = \int_{E_{\min}}^{E_{\max}} \sigma_i(E) \frac{F(E,z)}{E} \mathrm{d}E, \qquad (D.5)$$

where the ionisation cross sections σ_i are taken from Verner & Yakovlev (1995).

D.3.2. Secondary ionisations

Part of the kinetic energy of fast photoelectrons is lost by ionisations. These secondary ionisations are far more important for H, H_2 and He than direct ionisation. Dalgarno et al. (1999) calculate the number of ions N_{ion} produced for a given species i. For a given electron energy E, N_{ion} is given by

$$N_{\mathrm{ion}} = E/W, \qquad (D.6)$$

where W is the mean energy per ion pair. Dalgarno et al. (1999) calculated W for pure ionised H-He and H_2-He mixtures and parameterised W as:

$$W = W_0(1 + cx^\alpha), \qquad (D.7)$$

where W_0, c and α are given in Table 4 of their paper. The corrected mean energies for ionisation in the $H-H_2$-He mixture are given by

$$W(H^+) = W_{\mathrm{H,He}}(H^+) \left[1 + 1.89 \frac{n(H_2)}{n(H)} \right], \qquad (D.8)$$

$$W(H_2^+) = W_{H_2,\mathrm{He}}(H_2^+) \left[1 + 0.53 \frac{n(H)}{n(H_2)} \right]. \qquad (D.9)$$

The ionisation rate at depth z into the cloud for species i is then given by

$$\zeta_{i,\mathrm{sec}} = \int_{E_{\min}}^{E_{\max}} \sigma_{\mathrm{pa}}(E) F(E,z) \frac{E}{W} \mathrm{d}E \quad \mathrm{s}^{-1} \text{ per H nucleus.} \quad (D.10)$$

We rewrite this to a rate dependent on the fractional abundance of the species x_i:

$$\zeta_{i,\mathrm{sec}} = \int_{E_{\min}}^{E_{\max}} \sigma_{\mathrm{pa}}(E) F(E,z) \frac{E}{W x_i} \mathrm{d}E \quad \mathrm{s}^{-1} \text{ per species } i, \quad (D.11)$$

where x_i is the fraction of species i. Since we integrate over the range $1-10$ keV and W goes to a limiting value, we use the parameters applicable to the 1 keV electron. The ionisation rate then simplifies to:

$$\begin{aligned}
\zeta_{i,\mathrm{sec}} &= \frac{1 \text{ keV}}{W(1 \text{ keV})x_i} \int_{E_{\min}}^{E_{\max}} \sigma_{\mathrm{pa}}(E) F(E,z) \mathrm{d}E \qquad (D.12) \\
&= \frac{1 \text{ keV}}{W(1 \text{ keV})x_i} H_X \quad \mathrm{s}^{-1} \text{ per species } i.
\end{aligned}$$

We also include secondary ionisations for C, N, O, Si, S, Cl, Fe, C^+, N^+, O^+, S^+ and Fe^+. We scale the ionisation rate of these species to that of atomic hydrogen by

$$\zeta_i = \zeta_H \frac{\sigma_{\mathrm{ei},i}}{\sigma_{\mathrm{ei,H}}} \quad \mathrm{s}^{-1}. \qquad (D.13)$$

We integrate over the range $0.1-1.0$ keV to get an average value of the electron impact ionisation cross section σ_{ei}. Using the experimental data fits of Lennon et al. (1988). The scaling factors $\sigma_{\mathrm{ei},i}/\sigma_{\mathrm{ei,H}}$ for C, N, O, Si, S, Cl, Fe, C^+, N^+, O^+, S^+, and Fe^+ are 3.92, 3.22, 2.97, 6.67, 6.11, 6.51, 4.18, 1.06, 1.24, 1.32, 1.97, and 2.38, respectively.

D.3.3. FUV photons from secondary electrons

When energetic electrons created in X-ray ionisations collide with atomic and molecular hydrogen, H_2 Lyman-Werner and H Lyman α photons are produced, which can significantly affect the chemistry. The photoreaction rate R_i per atom or molecule of species i is given by

$$R_i = \frac{x_{H_2} \zeta_{H_2} p_m + x_H \zeta_H p_a}{1 - \omega} \quad \mathrm{s}^{-1}. \qquad (D.14)$$

The values of p_a are taken from Table 4.7 of Yan (1997) and values of p_m are the rates for cosmic-ray induced reactions from Le Teuff et al. (2000). There is an exception for CO, however, where we take the rate, corrected for self-shielding, given by Maloney et al. (1996):

$$R_{\mathrm{CO}} = 2.7 x_{\mathrm{CO}}^{-1/2} (T_k/1000)^{0.5} \zeta_{H_2} x_{H_2} \quad \mathrm{s}^{-1}. \qquad (D.15)$$

D.3.4. Vibrationally excited H_2

Vibrationally excited H_2 can enhance reactions with an activation barrier and also be an important heating or cooling source. To calculate the populations of the vibrational levels of H_2, we take into account:

- Collisions with fast electron produced by X-ray photo-ionisation.
- Collisions with thermal electrons, H, H_2 and He.
- Chemical destruction and production in chemical reactions.
- Radiative decay.

We use the results of Dalgarno et al. (1999) to calculate the X-ray induced excitation to the vibrational levels $v = 1$ and $v = 2$. The ratio of the yields $Y(v = 2)/Y(v = 1)$ is about 0.070. Excitation to higher levels is not taken into account, since the yield to higher levels decreases very rapidly. First we calculate the mean energy for excitation, W, in the H_2-He mixture. The parameters are listed in Table 5 of Dalgarno et al. (1999). The function W has the same form as Eq. (D.7). The mean energy for excitation also depends on the abundances of H and H_2. The yield has to be corrected with a factor $C(H,H_2)$, which is given by

$$C(H, H_2) = \frac{2n(H_2)}{n(H) + 2n(H_2)}, \qquad x \geq 10^{-4} \qquad (D.16)$$

$$C(H, H_2) = \frac{n(H_2)/n(H)}{n(H_2)/n(H) + a(x)}, \quad 10^{-7} < x < 10^{-4}$$

where $a(x) = 0.5(x/10^{-4})^{0.15}$. The rates for excitation by thermal electrons are taken from Yan (1997), who finds that the transitions rates for $H_2(v = 0)$ to $H_2(v = 1, 2)$ are given by

$$R(0 \to 1) = 9.7 \times 10^{-11}(T_k/300)^{0.87}$$
$$\times \exp(-6140/T_k) \qquad (D.17)$$

$$R(0 \to 2) = 7.5 \times 10^{-12}(T_k/300)^{0.91}$$
$$\times \exp(-11\,900/T_k). \qquad (D.18)$$

The excitation rate for the transition $v \to v + 1$ is taken to be v times the $0 \to 1$ rate. Excitations with $\Delta v > 1$ are not taken into account. The quenching rates are calculated through detailed balance. The quenching rates from $v \to v'$ by atomic hydrogen are given in Table 4.2 of Yan (1997) and are of the form:

$$R(v \to v') = \alpha(T_k/300)^{\beta} \exp(-\gamma/T_k) \text{ cm}^3 \text{ s}^{-1}. \qquad (D.19)$$

The excitation rates are obtained by detailed balance. For the molecular excitation and quenching rates we use the results of Tine et al. (1997). Collisions where either before or after one of the H_2 molecules is in the $v = 0$ state are considered. The rate coefficients are of the form:

$$\log_{10} R(v_1, v_1'; v_2, v_2') = A + B/T_k + C \log_{10} T_k, \qquad (D.20)$$

and are given in Table 1 of Tine et al. (1997), who also considered collisions with He. They give a rate coefficient for the $v = 1 \to 0$ transition:

$$\log_{10} R(1 \to 0) = -8.8T_k^{-1/3} - 16.5 \qquad T_k \leq 90 \text{ K} \qquad (D.21)$$
$$= -18.9T_k^{-1/3} - 14.2 \quad 90 < T_k \leq 230 \text{ K}$$
$$= -47.4T_k^{-1/3} - 9.4 \qquad T_k > 230 \text{ K}.$$

For the other transitions with $\Delta v = 1$, the same rates are used. The upward transitions can be obtained by detailed balance. Yan (1997) also calculated the dissociation and ionisation rates by thermal electrons and since the ionisation threshold is much higher than the vibrational energies one rate is used for all vibrational energies:

$$R_{e,diss} = 7.03 \times 10^{-9}(T_k/300)^{0.41} \exp(-118\,600/T_k) \qquad (D.22)$$
$$R_{e,ion} = 8.9 \times 10^{-10}(T_k/300)^{0.57} \exp(-179\,400/T_k). \qquad (D.23)$$

The dissociation rates by atomic hydrogen are given in Table 4.3 of Yan (1997), which are of the same form as Eq. (D.19). For the dissociation rates by H_2 we use the results of Lepp & Shull (1983), which are given by

$$R_{H_2,diss} = 6.29 \times 10^{-15} \qquad (D.24)$$
$$\times A \exp(1.44v - 0.037v^2)f(T_k)/f(4500 \text{ K}),$$

where $A = 1.38$, $f(T_k) = T_k^{0.5}\alpha \exp(-\alpha)$, $\alpha = [1+(E_{th}+1)/kT_k]$ and $E_{th} = 4.48 \text{ eV} - E(v)$. For the dissociative attachment reaction:

$$H_2 + e \to H + H^-,$$
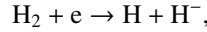
we use the results of Wadehra & Bardsley (1978) and the reaction rates have the same form as Eq. (D.19). Vibrationally excited H_2 can be destroyed in chemical reactions. Endothermic reactions with vibrationally excited H_2 can lower the activation barrier, by using the energy of the vibrational level. The barrier is reduced, but cannot become negative: $E' = \min(0, E - E(v))$. When H_2 is formed in chemical reactions which are exothermic, part of the formation energy goes into the excitation of the vibrational levels. Formation of H_2 on grains can play a very significant role. H_2 has a binding energy of 4.48 eV. Following Sternberg & Dalgarno (1989), we assume one third of this energy to be distributed statistically over all the vibrational levels:

$$x(H_2(v)) = \frac{\exp(-E(v)/1.493)}{\Sigma_v \exp(-E(v)/1.493)}, \qquad (D.25)$$

where $x(H_2(v))$ is the fraction of H_2 formed in vibrational state v. When H_2 formation reactions are endothermic, all the H_2 is in the ground vibrational state. When they are exothermic part of the energy is distributed statistically following Eq. (D.25). The Einstein A coefficients for radiative decay are taken from Turner et al. (1977). We take a weighted average over the rotational levels of each vibrational level, which we assume to be thermalised, to get an Einstein A coefficient for the decay from $v \to v'$.

Appendix E: Energy deposition rate per hydrogen nucleus

The photon energy absorbed per hydrogen nucleus, H_X, is given by

$$H_X = \int_{E_{min}}^{E_{max}} \sigma_{pa}(E)F(E, z)dE. \qquad (E.1)$$

The interval $[E_{min}, E_{max}]$ is the spectral range where the energy is emitted. The photoelectric absorption cross section per hydrogen nucleus, σ_{pa}, is given by

$$\sigma_{pa}(E) = \sum_i \mathcal{A}_i(\text{total})\sigma_i(E). \qquad (E.2)$$

Morrison & McCammon (1983) state that the X-ray opacity is independent of the degree of depletion onto grains. Therefore, we take the total (gas and dust) elemental abundances, $\mathcal{A}_i(\text{total})$, as given in Table 2 to calculate σ_{pa}. The X-ray absorption cross sections, σ_i, are taken from

Verner & Yakovlev (1995). The flux $F(E, z)$ at depth z into the cloud is given by

$$F(E, z) = F(E, z = 0) \, \exp(-\sigma_{\mathrm{pa}}(E) \, N_{\mathrm{H}}), \qquad (\mathrm{E.3})$$

where N_{H} is the total column of hydrogen nuclei and $F(E, z = 0)$ the flux at the surface of the cloud.